CHALMERS

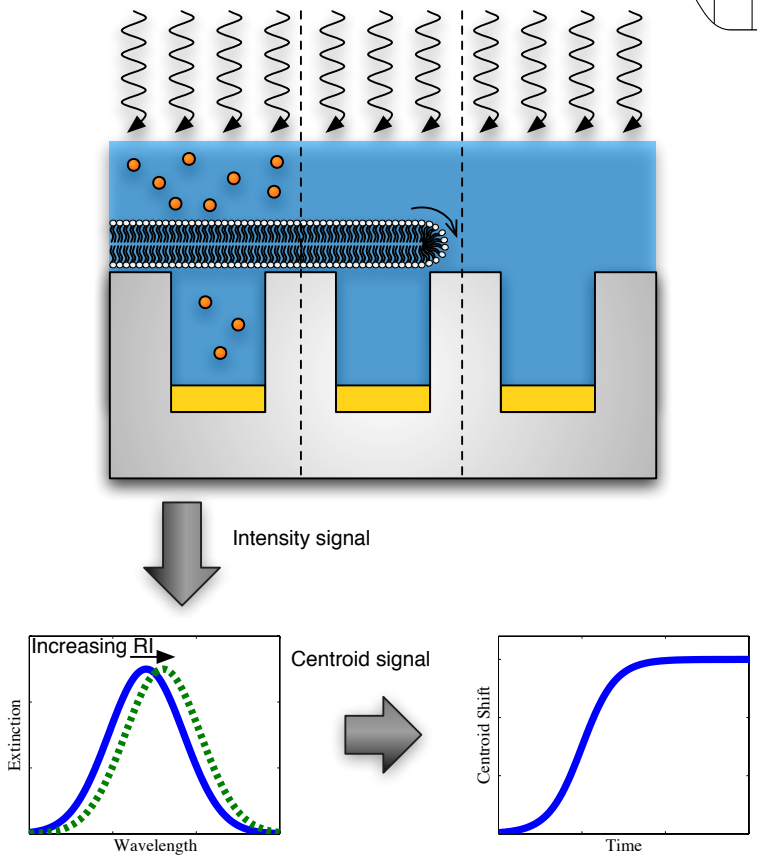

Nanoplasmonic and Fluorescence Microscopy Studies of Cell Membrane Mimics

Thesis for the Degree of Master of Science

Björn Johansson

Department of Applied Physics
Division of Biological Physics
Chalmers University of Technology
Göteborg, Sweden 2011

THESIS FOR THE DEGREE OF MASTER OF SCIENCE

Nanoplasmonic and Fluorescence Microscopy Studies of Cell Membrane Mimics

Björn Johansson

CHALMERS

Department of Applied Physics
Chalmers University of Technology
Göteborg, Sweden 2011

Nanoplasmonic and Fluorescence Microscopy Studies of Cell Membrane Mimics

Björn Johansson

Department of Applied Physics
Chalmers University of Technology
SE-412 96 Göteborg
Sweden
Telephone + 46 (0) 31-772 10 00

Cover illustration: Schematic illustration of a transport experiment with a lipid bilayer shear-driven across a nanostructured surface with embedded nanoplasmonic sensing elements.

Printed at Chalmers Reproservice
Göteborg, Sweden 2011

Nanoplasmonic and Fluorescence Microscopy Studies of Cell Membrane Mimics

Björn Johansson
Department of Applied Physics
Chalmers University of Technology

Abstract

Despite the fact that two thirds of all pharmaceuticals today target membrane proteins, we know rather little about them since the complexity of the cell membrane makes membrane proteins difficult to study. Furthermore, since membrane proteins control transport of molecules across cell membranes, it is also difficult to study such transportation processes.

In this thesis a method for studying transport of molecules across artificial cell membranes, via simultaneous fluorescence microscopy and localized surface plasmon resonance sensing (LSPR), has been developed. The method utilize shear-driven lipid bilayer cell membrane mimics, where hydrodynamic forces in a microfluidic channel introduced by bulk flow is used to move the bilayer. The bilayer is shear-driven over a nanostructured surface, producing a lipid bilayer spanning nanosized wells embedded in the surface. In the bottom of the wells are situated gold nanodisc nanoplasmonic sensing elements. The LSPR of the nanodiscs is sensitive to changes in the refractive index of the surrounding dielectric. The aim is that such a surface with embedded nanoplasmonic sensing elements in combination with a locally free spanning lipid bilayer will enable time resolved measurements of transport across the cell membrane mimic, into and out of the nanowells.

Keywords: nanoplasmonics, localized surface plasmon resonance, lipid bilayer, microfluidics, biosensor, artificial cell membrane, fluorescence microscopy

Contents

List of abbreviations

FRAP	Fluorescence recovery after photobleaching
LSP	Localized surface plasmon
LSPR	Localized surface plasmon resonance
PDMS	Polydimethylsiloxane
PECVD	Plasma enhanced chemical vapor deposition
POPC	1-palmitoyl-2-oleoyl-sn-glycero-3-phosphocholine
R-DHPE	Lissamine rhodamine B 1,2-dihexadecanoyl-sn-glycero-3-phosphoethanolamine
RIE	Reactive ion etching
RIU	Refractive index unit
SEM	Scanning electron microscope
SiO_2	Silicon dioxide
SLB	Supported lipid bilayer
SNR	Signal to noise ratio
SPP	Surface plasmon polariton
UV	Ultraviolet

Chapter 1:
Introduction

Cells, either in the shape of single cells or as a building block of something bigger, form everything living on this planet. One of the things that they share, and therefore everything living has in common, is a biological membrane. The biological membrane provides a barrier between the cell interior and exterior enabling for instance different chemical constituents on the inside versus the outside of the cell. This means that even though a biological membrane is only approximately 5 nm thick, it is very important indeed[1].

Incorporated into the biological membrane is a class of proteins known as membrane proteins, a very diverge class of proteins, performing a wide range of functions. The membrane proteins may serve as receptors for different types of signal factors or as pumps, e.g. pumping ions, which due to their charge are unable to readily pass the membrane[2].

Our knowledge of properties of membrane proteins get increasingly important these days since a growing number of drugs target membrane proteins specifically, with about two thirds of all drugs targeting membrane proteins today[3]. Even so, due to the difficulty associated with studying predominantly single aspects of membranes and membrane proteins, owing to the diversity of lipids and proteins naturally occurring in the membrane, we still know rather little about them[4].

One of the most used techniques for studying biological membranes is using the supported lipid bilayer (SLB) model system[5]. This model system, being a membrane mimic, will however never give the exact behavior of the real system, rather provide a small insight. In this thesis the SLB model system has been used as one part of a setup developed in order to perform transport measurements across a biological membrane mimic. Further on, the aim is to perform measurements of transport properties of real biological membranes.

The concept of shear-driven lipid bilayers is crucial to the work performed in this thesis. A bilayer can be moved across a surface using hydrodynamic shear forces introduced by a bulk flow above the bilayer[6]. Through the use of a microfluidic[7;8] device, which due to the small geometry (the channel cross section is on the order of $10^{-8}\,\mathrm{m}^2$) ensures a laminar flow and thus easily controllable bulk flow, the motion of the bilayer can be controlled.

The purpose of this thesis work is to combine fluorescence microscopy, commonly used to study SLB systems, with localized surface plasmon resonance (LSPR) biosensing. This means incorporation of a LSPR sensing element in the microfluidic device mentioned previously. The LSPR sensing element is a large number of gold nanoparticles made using colloidal lithography. The LSPR of metal nanoparticles is very sensitive to changes in the

dielectric function of the dielectric surrounding the nanoparticle. Since biological material in general has a larger refractive index, and therefore a larger dielectric function, than water, the LSPR concept is very well suited for biosensing[9].

The aim is to be able to use the setup developed during this thesis to perform measurements of single aspects of e.g. transport properties of membrane mimics and membrane proteins. What differs this work from setups already used and commercially available[10], is the comparatively large liquid reservoirs either side of the membrane. The large reservoirs enables time resolved measurements which can yield a better insight into membrane transport properties.

Below is a short summary of the chapters included in this thesis. In short the thesis starts of with a background description and a description of the methods used to produce the results found later on in the thesis. The last part contains a discussion of the work done.

- ◇ **Chapter 2** provides a short introduction to lipids, properties of amphiphilic molecules and an introduction to the SLB model system used in this thesis.
- ◇ The theory behind LSPR is provided in a condensed form in **chapter 3**. Along with the theory of LSPR a background discussing optical properties of metals and surface plasmon polaritons (SPPs) is also provided.
- ◇ **Chapter 4** contains a presentation of the methods used during the thesis, ranging from nanofabrication to the operation of the LSPR setup.
- ◇ In **chapter 5** the results produced during the thesis are presented.
- ◇ The last part of the thesis, **chapter 6**, provides a discussion of the work, what has been done, what has not and what can be done to improve the method in the future.

Chapter 2:

Lipids and bilayers

Lipids are the main building block of biological membranes and is a group of molecules that include among others, phospholipids, cholesterol and fat. In this thesis a subgroup of phospholipids called glycerophospholipids, from here on referred to as lipids, have been studied. This class of lipids are among the most commonly found in biological membranes, and consist of a glycerol skeleton with a hydrophilic head group based on phosphate group, while two hydrocarbon chains, typically one saturated and one unsaturated in *cis*-conformation, form a hydrophobic tail[11]. The constituents of the glycerophospholipid 1-palmitoyl-2-oleoyl-sn-glycero-3-phosphocholine (POPC) can be seen in Fig. 2.1. For the course of this thesis two different glycerophospholipids have been used, POPC which is a standard lipid with a zwitterionic head-group present in large quantities in biological membranes, and lissamine rhodamine B 1,2-dihexadecanoyl-sn-glycero-3-phosphoethanolamine (R-DHPE), a lipid with a fluorescence tag attached to the negatively charged head-group. The structure of these lipids and their chemical formula can be seen in Fig. 2.2.

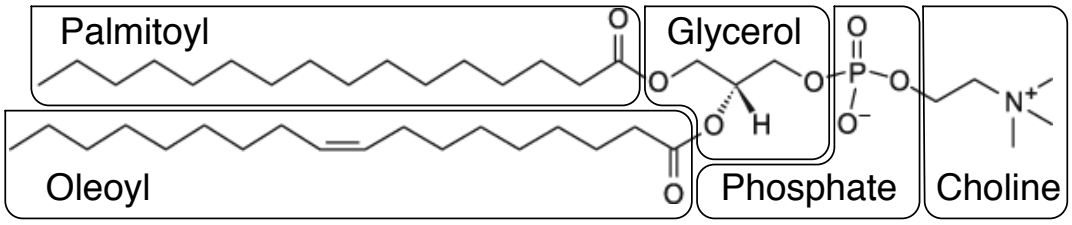

Fig. 2.1: *The chemical composition of the glycerophospholipid POPC, with indications of the different groups in the molecule. The polar head-group consist of the phosphate together with choline. The glycerol molecule is the lipid backbone while the apolar hydrocarbon chains constitute the hydrophobic tails.*

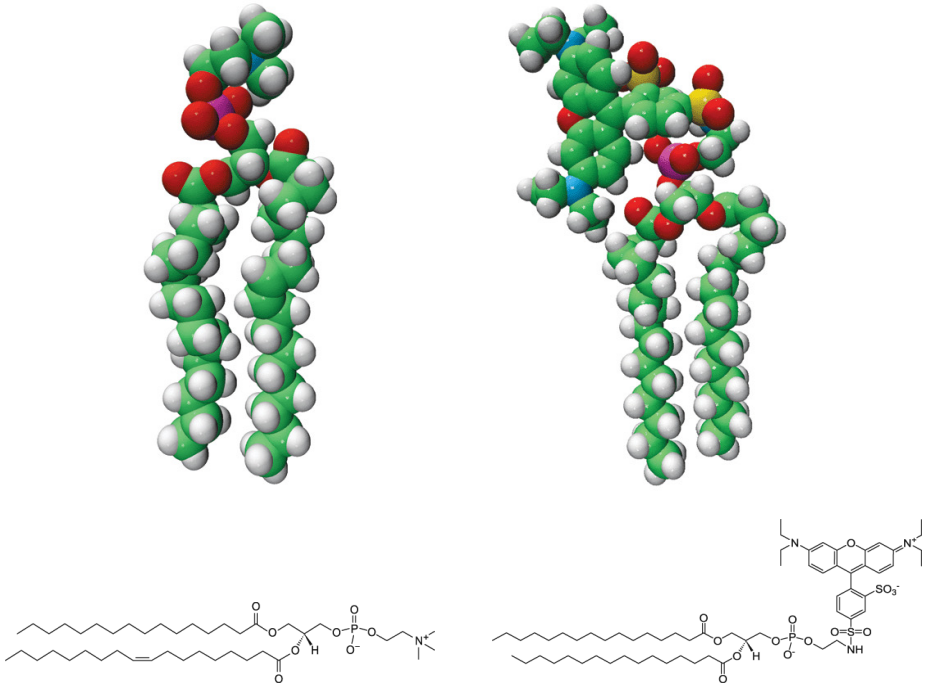

(a) POPC (b) R-DHPE

Fig. 2.2: *The molecular structure and chemical formula of (a) POPC and (b) the fluorescence labeled R-DHPE, the two lipids that have been used for the studies in this thesis. Images from:* `http://www.avantilipids.com/images/catalog/2011AvantiCatalog.pdf`.

2.1 Critical packing parameter and lipid aggregates

Lipids in an aqueous solution will, due to their amphiphilic properties, form different aggregates. The type of aggregate varies between micelles (i.e. spheres or cylinders), inverted micelles and bilayers, and is in principle determined by three simple parameters; the *optimum head-group area* a_0, the *critical chain length* l_c and the *hydrocarbon volume* v. The optimum head-group area corresponds to the distance between amphiphilic molecules that minimizes the free energy. A too large distance mean that the hydrophobic hydrocarbon chains are forced into contact with the surrounding water molecules, while too small distance mean that the head-groups repel each other due to for instance electrostatic forces. The critical chain length is the length of the hydrocarbon chain, in a fully extended configuration, while the hydrocarbon volume simply is the volume of the hydrocarbon chains. From these parameters it is possible to determine the critical packing parameter[12]:

$$cpp = \frac{v}{l_c a_0}. \tag{2.1}$$

The value of *cpp* determines the shape of the self assembled structure in an aqueous solution with $cpp \leq 1/3$ corresponding to spherical micelles, $1/3 < cpp \leq 1/2$ corresponding

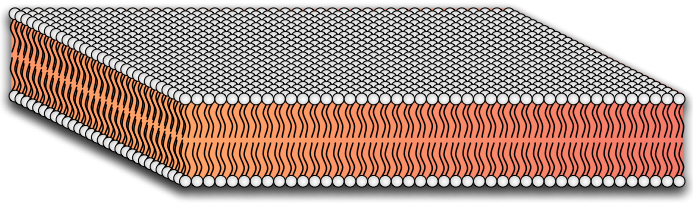

Fig. 2.3: *Schematic illustration of amphiphilic lipids forming a bilayer with the hydrophilic head-groups outwards and the hydrophobic tails inwards.*

to cylindrical micelles, $1/2 < cpp \leq 1$ corresponding to bilayers and finally $cpp > 1$ corresponding to inverted micelles[12–14].

Due to their small head-groups and large hydrocarbon volume combined with a small critical chain length, a combination achieved from having dual hydrocarbon chains, phospholipids have $1/2 < cpp \leq 1$ and will preferably form bilayers when present in an aqueous solution.

A bilayer is a two dimensional sheet of lipids arranged in two leaflets, so that the head-groups are in contact with the surrounding aqueous solution while the inside of the bilayer is hydrophobic, see Fig. 2.3. A spherical bilayer is called a vesicle and can be described as a lowest order mimic of a biological cell in that the inside of the vesicle is protected from the outside by an amphiphilic bilayer membrane. The bilayer aggregate exist in both single bilayer, so called unilamellar, and multi bilayer, multilamellar, structures[12]. In this thesis only the former structure will be of interest, in the form of unilamellar vesicles, or liposomes, and lipid bilayers on a solid support, described later in this chapter.

2.2 Biological membranes and the SLB

Biological membranes are one of the most important building blocks of everything living, being the barrier between the cell and the surroundings but also a boundary of the cell organelles. Biological membranes are built up mainly by a lipid bilayer consisting of more than 1000 different lipids[11]. Bound to the membrane or spanning the membrane are a class of proteins called membrane proteins. Those proteins regulate many of the processes in the cell, and, for instance they control the ion concentration in the cell. Many illnesses can be linked to malfunction of membrane proteins and it is believed that viruses enter the cell through interaction with membrane proteins[1].

The complexity of real biological membranes with lipids, proteins and carbohydrates, and the membrane interaction with the cellular skeleton and extracellular matrix as well as the curvature of the cell make direct investigations of specific aspects of biological membranes, such as properties of a single protein or the membrane as such, very difficult[5]. However, much knowledge of real biological membranes can be gained from the study of model systems, e.g. artificial lipid bilayers[5;15;16].

A commonly used model system is a lipid bilayer on a solid support, SLB. An SLB

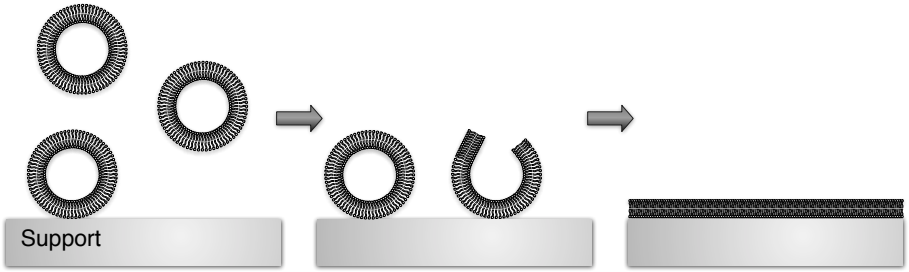

Fig. 2.4: *Schematic illustration of the formation of an SLB. From vesicles in bulk, via adsorption of vesicles to a support and the rupture of vesicles, to the final lipid bilayer on a support.*

can be formed by vesicles adsorbing to the surface then bursting into an SLB, see Fig. 2.4. The SLB is built up by two sheets of lipids on a solid support. Each of those sheets can be described as a two dimensional liquid with a diffusibility[5]. The amphiphilic nature of both the lipids and the bilayer as such provide a barrier against intersheet diffusion. The sheets are connected at the edges where the lipids form a semicircle between the sheets to keep water out of the hydrophobic bilayer interior. However, the energy associated with a lipid being on an edge is larger than the energy of a lipid in the flat regime. The bend push the hydrophilic head-groups apart, forcing the hydrophobic hydrocarbon chains into contact with the surrounding water. Additionally, the bend causes the hydrocarbon chains too close, in turn causing steric hindrance, further increasing the energy associated with a lipid on the edge[12]. See the right part of Fig. 2.5 for a schematic illustration of a bilayer edge.

The SLB model system works well for studying lipid-interactions within the bilayer and properties like the fluidity of a bilayer. Even though a thin liquid film is formed between the bilayer and the support, this is generally not sufficiently thick for membrane spanning proteins not to be in contact with the support. The interaction between protein and surface that is created may influence the properties of the protein. One solution to avoid this is the use of a polymer cushion between the SLB and the solid support, distancing the bilayer from the solid support[4].

In order for the transport to take place during a long enough time to make time resolved measurement of the transport, thus extruding more information from the experiments, a large liquid reservoir is required on both sides of the SLB. This has been handled using a nanostructured surface, providing nanowells as reservoirs beneath the SLB. Also, since the SLB is locally free spanning this means that if and when proteins are incorporated into the bilayer, they will not be in direct contact with the support above the wells.

2.3 Shear-driven bilayers

With the SLB being built up by two sheets of lipids, not in direct contact with each other, it is possible to move one of the sheets in relation to the other. The corresponding rolling movement of the bilayer can be likened to that of a caterpillar band. The force required to move for instance the upper sheet in relation to the lower can be achieved by the hydrodynamic force, σ_{hydro}, introduced by a bulk flow above the bilayer[6]. The use of a microfluidic channel enables, due to the laminar flow profile in the channel, easy moderation of the hydrodynamic force on the bilayer by moderation of the bulk flow speed within the channel[6].

A schematic illustration of a shear-drive lipid bilayer on a solid support is shown in Fig. 2.5, where σ_{hydro} is the hydrodynamic shear force, b is the intermonolayer frictional coefficient, b_{ls} is the frictional constant between the lower leaflet and the support. v_{u}, v_{l} and v_{f} are the velocities of the upper and lower monolayer and the bilayer front respectively. Fig. 2.5 give the following expressions for the velocities of the upper and lower monolayers[17]

$$v_{\text{u}} = \sigma_{\text{hydro}} \left(\frac{1}{b} + \frac{1}{b_{\text{ls}}} \right) \tag{2.2}$$

$$v_{\text{l}} = \frac{\sigma_{\text{hydro}}}{b_{\text{ls}}}. \tag{2.3}$$

Since the no-slip conditions dictates that the velocity of a fluid relative to the surface should be zero at the fluid-surface boundary, the bulk flow velocity will be larger in the center of the channel than at the walls[18]. This means that the hydrodynamic shear-force will be larger, and thus that the velocity of the monolayers will differ across the channel width. The average velocity of the advancing bilayer front can be determined as[6]

$$v_{\text{f}} \approx \frac{\langle v_{\text{u}} \rangle + \langle v_{\text{l}} \rangle}{2}, \tag{2.4}$$

where $\langle v_{\text{u}} \rangle$ and $\langle v_{\text{l}} \rangle$ describes the average velocity of the upper and lower monolayer across the channel width respectively. Jönsson et al.[6] has shown that in fact the lower monolayer

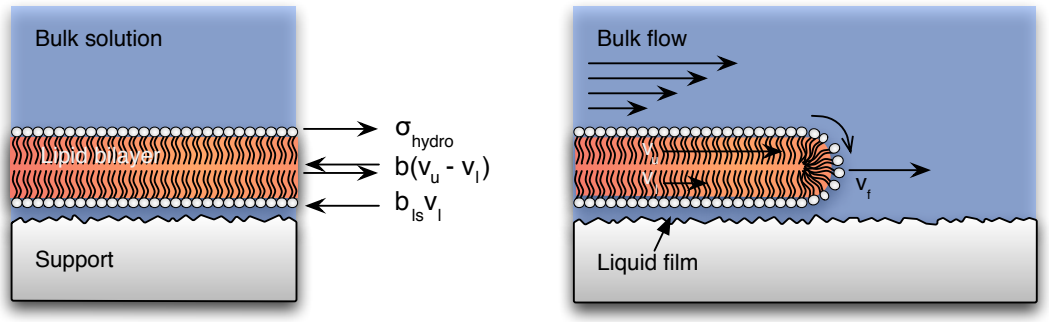

Fig. 2.5: *Schematic illustration of a shear-driven lipid bilayer on a solid support, with representations of the forces acting on the bilayer and the velocities of the bilayer.*

is almost stationary, corresponding to

$$v_{\mathrm{u}} \approx \frac{\sigma_{\mathrm{hydro}}}{b} \tag{2.5a}$$

and

$$v_{\mathrm{f}} \approx \frac{v_{\mathrm{u}}}{2}. \tag{2.5b}$$

This is only a short summary of the theory behind shear-driven lipid bilayers, for a more in-depth view, see Jönsson et al.[6] and[17].

Just like the bulk flow velocity changes across the channel width it changes across the channel height. Thus molecules extending further into the bulk will experience a larger flow speed, therefore a larger hydrodynamic force and thus move faster than the rest of the bilayer[17;19]. Additionally, it is energetically unfavorable for molecules extending beyond the surrounding bilayer to fit in the lower monolayer. These two effects combine into an accumulation of larger molecules in the bilayer front[6] and has been used for instance to separate proteins incorporated in a bilayer based on size[19].

An SLB can form on a glass support but on very few other surfaces[20], making it difficult to perform experiments with an SLB on for instance gold surfaces. Additionally, forming an SLB on the nanostructured surface discussed later in this thesis, will not yield the desired locally free spanning lipid bilayer. The concept of shear-driven bilayers offer an advantage in this respect, since it is possible to form a bilayer on one type of support, e.g. glass, and the shear-drive the bilayer across the surface of interest, whether it being made of e.g. gold or nanostructured[21]. Additionally, a shear-driven bilayer offers the possibility to form a locally free spanning lipid bilayer over a nanostructured surface, such as the one discussed in this thesis[21].

Chapter 3:
Surface plasmons

In this chapter a short review of the theory behind LSPR is provided along with a brief introduction to surface plasmon polaritons (SPPs). However, the chapter starts with a short introduction into electromagnetic radiation and the optical properties of materials and metals.

3.1 Electromagnetic radiation and optical properties of metals

Electromagnetic radiation is classified with respect to energy, wavelength and frequency. Visible light constitute only a very small fraction of the electromagnetic spectrum, which ranges from radiowaves, via microwaves, infrared, visible, ultraviolet and X-rays, to γ-rays, see Fig. 3.1. As with all electromagnetic radiation, visible light is mediated via photons, the electromagnetic quanta, being discrete packets of energy[22].

The optical properties of a material, e.g. reflectivity, transmittance and refractive index, is determined by the interaction between photons and the valence electrons in the material. Metals have two characteristic properties that man has used for thousands of years, their luster and color. Goethe once wrote in his *Treatise on Color* that "If the color blue is removed from the spectrum, then blue, violet and green are missing and red and yellow remain." This is part of the explanation of why gold has the color of gold. Light transmitted through thin gold films is bluish-green, while light reflected from a gold surface is reddish-yellow. This, among other aspects, can be explained through the theory behind the optical properties of metals[22].

The interaction between light and the valence electrons in a material is described by the dielectric function, ε, which in general is complex and dependent on frequency, ω. The dielectric function can thus be divided into a real and a complex part,

$$\tilde{\varepsilon}(\omega) = \varepsilon_1(\omega) + i\varepsilon_2(\omega) \tag{3.1}$$

where ε_1 is the real part and related to the energy stored within the material and ε_2 is the complex part, related to the dissipation of energy within the material[9;22].

From Drude theory, the dielectric function of metals can be determined to[22]

$$\tilde{\varepsilon}(\omega) = 1 - \frac{\omega_{\mathrm{p}}^2}{\omega^2 - i\omega\omega_{\mathrm{d}}}, \tag{3.2}$$

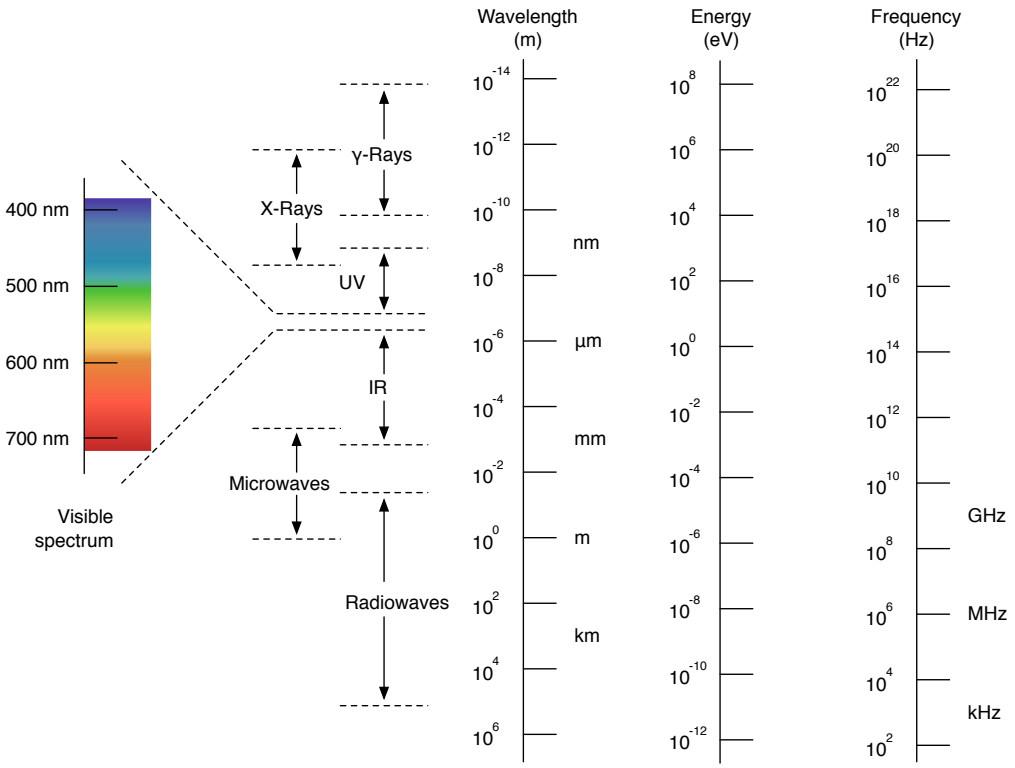

Fig. 3.1: *The electromagnetic spectrum. As can be seen, the part of the spectrum visible to the human eye, only constitute a very small fraction of the entire spectrum.*

where a plasma frequency, ω_p, and a damping frequency, ω_d, defined as[9;22]

$$\omega_\mathrm{p} = \sqrt{\frac{e^2 N_\mathrm{f}}{\varepsilon_0 m}} \tag{3.3a}$$

$$\omega_\mathrm{d} = \frac{\varepsilon_0 \omega_\mathrm{p}^2}{\sigma_0}, \tag{3.3b}$$

where e is the electron charge, N_f is the density of free electrons, ε_0 is the permittivity of vacuum, m is the electron mass and σ_0 is the dc-conductivity, have been introduced.

For the color of metals, the plasma frequency is of particular interest. This frequency describes the frequency boundary in the plasma model[22], briefly described later, above which the the metal is effectively transparent. For most metals, this plasma frequency is far into the ultraviolet range of the spectrum, making them reflect all visible wavelengths approximately equally, rendering them silvery. Some metals, such as gold and copper, have much lower plasma frequencies, making them better reflectors for lower frequencies. The reflectance spectrum is thus weighted more to the lower frequencies giving these metals a reddish-yellow color[22;23].

The dielectric function according to Drude theory, (3.2), can be expressed as the so called Drude equations for the optical constants, connecting the dielectric function with

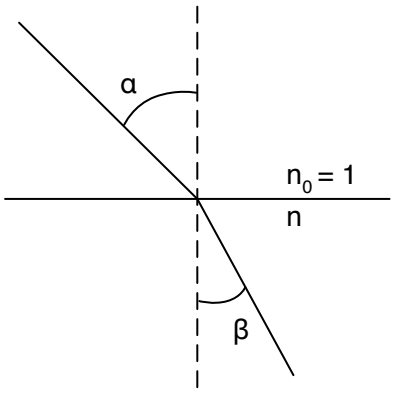

Fig. 3.2: *Refraction of a light beam passing from one material with refractive index n_1, into an other with refractive index n_2.*

the more commonly known (complex) index of refraction, $\tilde{n} = n + i\kappa$[9;22],

$$n^2 - \kappa^2 = \varepsilon_1 = 1 - \frac{\omega_\mathrm{p}^2}{\omega^2 + \omega_\mathrm{d}^2} \tag{3.4a}$$

and

$$2n\kappa = \varepsilon_2 = \frac{\omega_\mathrm{d}}{\omega}\frac{\omega_\mathrm{p}^2}{\omega^2 + \omega_\mathrm{d}^2}. \tag{3.4b}$$

The real part of the index of refraction, commonly referred to as the refractive index, can be determined from Snell's law[22]

$$n = \frac{\sin\alpha}{\sin\beta} \tag{3.5}$$

describing the refraction of a beam of light when passing into a material from vacuum, see Fig. 3.2. The refractive index of vacuum, n_0, is arbitrarily set to unity[22]. Additionally, the refractive index is related to the speed of light in the material according to[22]

$$n = \frac{c}{v} \tag{3.6}$$

where c is the speed of light in vacuum and v is the speed of light within the material. So far, no assumptions has been made regarding the size of the metal, meaning that the expressions stated above are equally true for a metal nanoparticle.

3.2 Localized surface plasmons

A metal can, to lowest order, be described as a mobile electron gas of conduction electrons moving through a fixed positive background of nuclei and core electrons, which has a resonance frequency that is the plasma frequency in equation (3.3a). Electromagnetic radiation

incident on a metal surface can couple with the free electrons of the metal in a so called SPP[9], first predicted in 1957 by Ritchie[24]. Slightly more than a decade passed between the first prediction of the SPP to the first successful excitation of SPPs by Kretschmann and Raether[25] and Otto[26]. The two setups are rather similar, a schematic illustration of the Kretschmann configuration is shown in Fig. 3.3(a). In the Kretschmann configuration a metal film with a thickness less than the wavelength of the light source used, is placed with a glass substrate on one side and another dielectric on the other. If the incident photon hits the metal interface through the glass substrate under total internal reflection, this gives rise to an evanescent field on the interface. This evanescent field will, in turn, excite a SPP on the metal/dielectric interface, given that the dielectric have an index of refraction sufficiently lower than the glass and the angle of incidence is in the right regime. For a more comprehensive review of the theory behind SPPs, see for instance Zayats et al.[27]

Nanoparticles, such as the ones fabricated during this thesis, are too small to facilitate enough space for a SPP to propagate, which means that it is impossible to excite a SPP in a nanoparticle. Instead, incident electromagnetic radiation can couple with the free electrons into a localized surface plasmon (LSP)[28], see Fig. 3.3(b).

When electromagnetic radiation interacts with, e.g., a spherical metal nanoparticle, it will induce a dipole moment proportional to the applied field with a proportionality constant, the polarizability[9],

$$\alpha = 4\pi a^3 \frac{\tilde{\varepsilon} - \varepsilon_\mathrm{d}}{\tilde{\varepsilon} + 2\varepsilon_\mathrm{d}}, \tag{3.7}$$

where a is the radius of the nanoparticle and ε_d is the dielectric constant of the dielectric. For metals, $|\varepsilon_1| \gg \varepsilon_2$ in the visible part of the spectrum[9], and thus the polarizability may be rewritten into[9]

$$\alpha = 4\pi a^3 \frac{\varepsilon_1 - \varepsilon_\mathrm{d}}{\varepsilon_1 + 2\varepsilon_\mathrm{d}}. \tag{3.8}$$

which has a maximum at the so called Fröhlich condition,

$$\varepsilon_1 = -2\varepsilon_\mathrm{d}, \tag{3.9}$$

corresponding to resonance condition of the LSP, or the LSPR. From (3.9) it is clear that the resonance frequency of (3.8) is strongly dependent on the dielectric environment. If ε_d increases the wavelength of the resonance frequency increases, i.e. the resonance frequency red shifts which can be used for sensing[9].

LSPR leads to both scattering and absorption of photons, which in the far field combine into a quantity called extinction. The probability of extinction is described by the optical cross section which describes the wavelength dependent effective area

$$\sigma_\mathrm{ext} = \sigma_\mathrm{sc} + \sigma_\mathrm{abs} \tag{3.10}$$

where σ_ext is the total extinction cross section and σ_sc and σ_abs are the cross sections of scattering and absorption, respectively. The optical extinction cross section of extinction

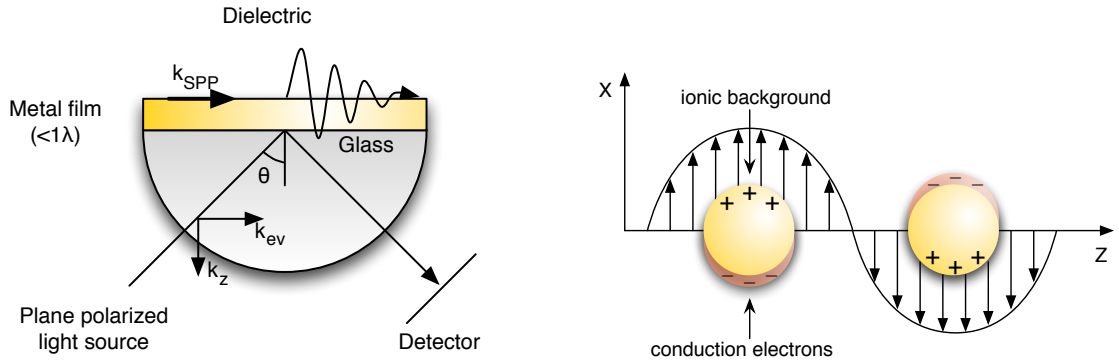

(a) Kretschmann configuration

(b) Light interaction with nanoparticle

Fig. 3.3: *Schematics of the Kretschmann configuration used to excite SPPs and of light interacting with a nanoparticle respectively. In (b) the the electron cloud of the nanoparticle is oscillating with respect to the ionic core due to the applied electromagnetic field.*

for metal particles can be deduced from Mie theory. For small spherical metal particles, $a \ll \lambda$, Mie theory predicts[9;27;29;30]

$$\sigma_{\text{ext}} = \frac{12\pi a^3 \omega}{c} \varepsilon_{\text{d}}^{3/2} \frac{\varepsilon_2}{[\varepsilon_1 + 2\varepsilon_{\text{d}}]^2 + \varepsilon_2^2}. \tag{3.11}$$

It is clear that this equation, given only small variations of ε_2 with respect to ω, describes peak extinction at the LSPR that is the Fröhlich condition in (3.9). From this equation it is also clear that the imaginary part of the dielectric function determines the width of the exctinction peak, with a smaller value of ε_2 corresponding to a narrower peak.

The theory described so far has only dealt with spherical nanoparticles, since it is by far the easiest geometry and one of the few for which the optical cross section is actually possible to derive analytically. The nanoparticles handled in this thesis are however not spherical but rather discs. By approximating a disc with an oblate spheroid, hence introducing principal axes and geometrical factors, it is possible to deduce an expression similar to (3.11)[9]. This derivation however is beyond the scope of this thesis.

3.3 Biosensing with plasmons

As previously mentioned, the LSPR is highly dependent on the dielectric function of the dielectric surrounding the nanoparticle, and such nanoparticles may therefore be used for sensing purposes. Since almost all biological matter have a refractive index, and thus a dielectric function, larger than that of water, LSPR is well suited for biosensing[31–33].

Because of this and other applications, a lot of different geometries have been investigated, ranging from spheres[34] via ellipsoids[35] to triangles[36;37] and other more elaborate structures such as cavities[38–40] etc. Also nanoparticles have been investigated both in a liquid suspension and deposited onto different supports[27;30;36;41;42].

In the application of biosensing there is a slight controversy between the sensor yielding the best possible signal and detection of low concentrations of biomolecules. However, using a surface inert to unspecific binding and a small surface coverage of nanoparticles, this controversy may be dealt with[43].

Chapter 4:
Method development

In this chapter an in depth view of the methodology used and developed during this thesis is presented, ranging from nanofabrication and chip construction to the different types of microscopy and sensing techniques used as well as the setup for combined LSPR and fluorescence microscopy measurements and routines to form an SLB in the microfluidic chips.

4.1 Fabrication

Performing fluorescence microscopy and LSPR biosensing simultaneously requires use of a sample that is suitable for both types of experiments. The basis of this sample is a microfluidic device, as developed by Jönsson et al.[21], which combines both a flat silicon dioxide (SiO_2) support where an SLB can be formed and a nanofabricated area for biosensing. There are several different steps involved in the fabrication of such a device, which means that a large part of the work in this thesis has been learning to master several different fabrication routines. These includes nanofabrication in the MC2 clean room at Chalmers as well as polymer molding in order to create the microfluidic channels.

In this section the main steps involved in the fabrication are described along with brief motivations as to why these steps are important.

4.1.1 Making holes

The first step of the sample fabrication is to incorporate an LSPR sensing element in a glass slide suitable for studies of an SLB. The LSPR sensing element is a large number of nanosized gold discs located at the bottom of similarly nanosized wells which has been etched in the glass slide. The nanodiscs and nanowells are made using a modified version of colloidal lithography**??**. For a schematic illustration of the colloidal lithography process, see Fig. 4.1. The process starts with a glass slide and a cleaning protocol. After cleaning a layer of SiO_2 is deposited on the surface using plasma enhanced chemical vapor deposition (PECVD). The deposition of SiO_2 is crucial since the etching, done in a later step, is not as efficient on glass.

The colloidal lithography starts with deposition of polystyrene spheres on the surface. The location of the spheres will in the end correspond to the location of the nanowells.

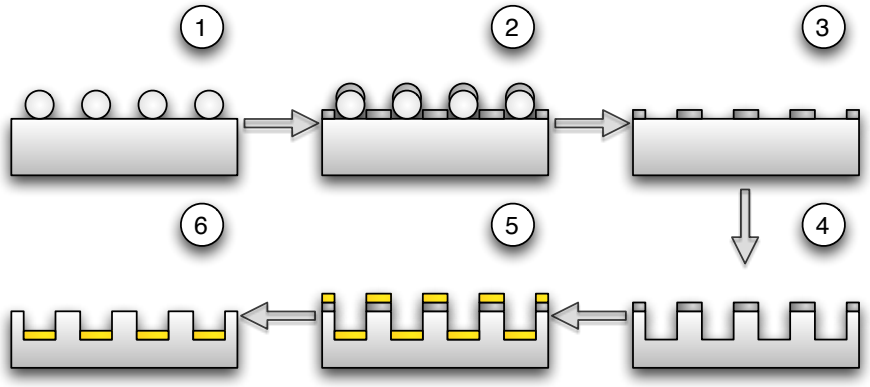

Fig. 4.1: *Schematic illustration of colloidal lithography. First colloids are deposited on the surface (1), then chromium is deposited (2) forming an etch mask when the colloids have been removed (3). Wells are then etched where the colloids once were (4) and gold is deposited on the surface (5). Finally chromium etching removes chromium and gold on the top surface (6).*

Therefore the spheres are supposed to be distributed uniformly across the surface. The electrostatic repulsion between the spheres will create a short range order between the spheres, but there will be no long range order. By charging the surface with a salt (aluminum chlorohydrate, ACH), an electrostatic attraction between the surface and the colloids is created which help the colloids to adsorb to the surface.

Next chromium is evaporated onto the surface using thermal evaporation. The subsequent tape lift-off will remove all colloids together with the chromium evaporated onto them, thus leaving a chromium surface with cavities in it where the colloids used to be. Since the final product is supposed to have holes incorporated into the SiO_2, the following step is to etch holes in the SiO_2 layer. The method used to etch is reactive ion etching (RIE) with NF_3 gas. RIE is only effective in the absence of chromium and thus the evaporated chromium forms an effective etch mask for milling holes into the SiO_2 where the polystyrene colloids once were.

The nanofabrication is now almost completed. The last step is to create the gold discs. Since gold does not stick to SiO_2, a thin layer of chromium must first be evaporated to ensure that gold sticks where it is supposed to, in the bottom of the wells. This layer must be really thin, since the next, and last, step is to remove the chromium using chromium wet etch. The thin layer of chromium under the gold discs in the bottom of the wells will not be reached by the etching agent, thus the gold discs will remain. All other chromium will be dissolved and the gold not in the wells will detach from the surface. Since liposomes will not merge into an SLB on gold surfaces[20], it is extremely important that all the gold not situated in the wells is removed from the surface. The result of this manufacturing process is a surface with a structure like that in Fig. 4.2(a) and 4.2(b). The corresponding extinction spectra of 110/30 nm discs can be seen in Fig. 4.3. For a short step-by-step guide to the nanofabrication in this thesis turn to Appendix A on page 43.

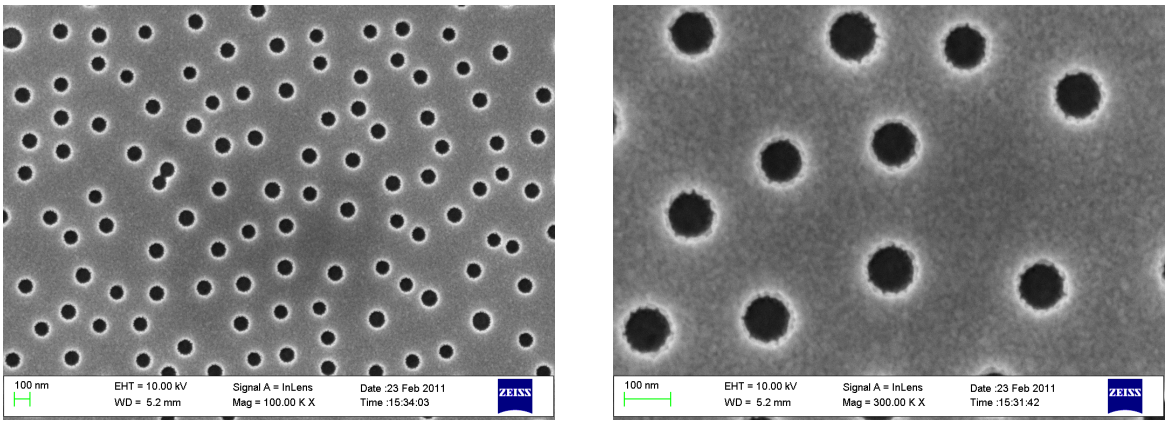

(a) 100 000 x (b) 300 000 x

Fig. 4.2: *In (a) and (b) are scanning electron microscope (SEM) images of the surface structure at 100k and 300k times magnification respectively. In these images one can see both the size of the wells and the distribution of wells across the surface. The size of the wells. The wells are approximately 100 nm in diameter and the average distance between the wells is approximately 250 nm.*

4.1.2 Building a channel

With the nanostructure done, the glass slides are ready to be used as the bottom of a microfluidic channel. The top of the channel is molded in polydimethylsiloxane (PDMS) using a silicon master with a channel forming protrusion, see Fig. 4.4(a). By pouring PDMS and curing agent onto the master and bake it in the oven a channel is formed. The channel is then attached to the glass surface after both surfaces have been treated in an oxygen plasma cleaner. The oxygen plasma cleaner effectively removes organic residues from the surface, including the methyl group usually present on the surface of PDMS. Removing the methyl group leaves a silane group on the surface, which will form a covalent bond with the glass surface. The attachment of the channel to the glass slide is thus non-reversible.

With the chip still sealed from the outside, connections must be attached to the channel. The connections are made out of silicone tubing that is glued to the channel connection chambers, see Fig. 4.4(b). When the connections are in place the chip is ready for measurements. A short step-by-step guide for channel molding and attachment is provided in Appendix B on page 45.

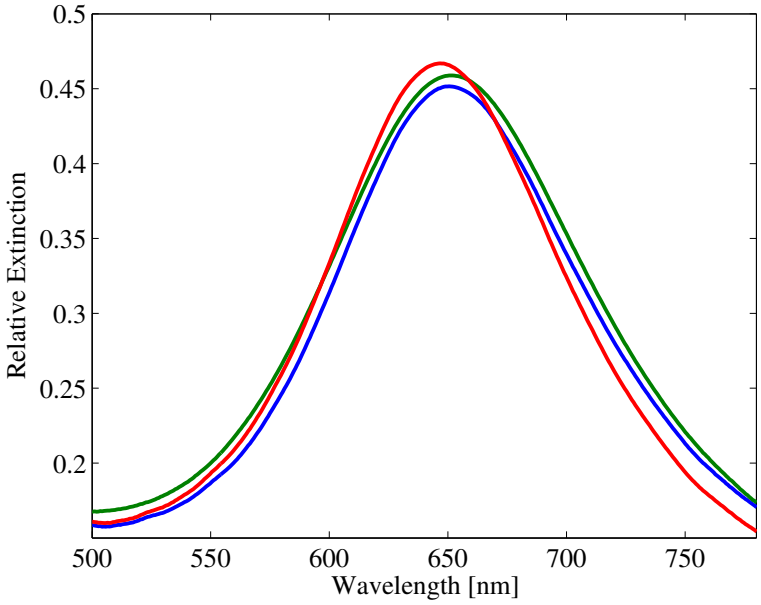

Fig. 4.3: *The extinction spectra of three nanofabricated surfaces. These samples contain 110/30 nm gold discs in 200 nm deep wells. This gave a peak extinction wavelength of ∼650 nm.*

4.2 Bilayer formation

When forming an SLB in the microfluidic chip, see Fig. 4.5 for a schematic illustration of the setup, liposomes are injected into connection 1. of the chip, while buffer is injected into 4. Connections 2. and 3. are outlets, i.e. the valves are open. Some of the liposomes in the solution will adsorb on the bottom of the channel, see Fig. 4.6(a). At a critical surface coverage, the vesicles will, depending on the surface chemistry and e.g. salt concentration and pH of the buffer solution[44], rupture into an SLB. An SLB will form on glass surfaces, but very few other materials. On many other surfaces, for instance gold, the vesicles will only adsorb, never form an SLB[20]. The surface chemistry of the glass can be altered if there are any residues from the fabrication, decreasing the SLB forming performance of the surface. If an SLB is formed in the channel, the result looks like Fig. 4.6(b). When the SLB has formed, the valves in 2. and 3. are closed and the alternative routing of the tubing from 4. (the dashed line in Fig. 4.5) is used, the liposomes are exchanged for buffer solution and the flow speed is increased in order to shear-drive the bilayer.

4.2.1 Why shear-driven lipid bilayers?

The main reason for performing measurements in a microfluidic channel is the concept of shear-driven lipid bilayers as developed by Jönsson et al.[6;21;45]. The main advantage of shear-driven bilayers is the possibility to move the bilayer across a surface and thus have

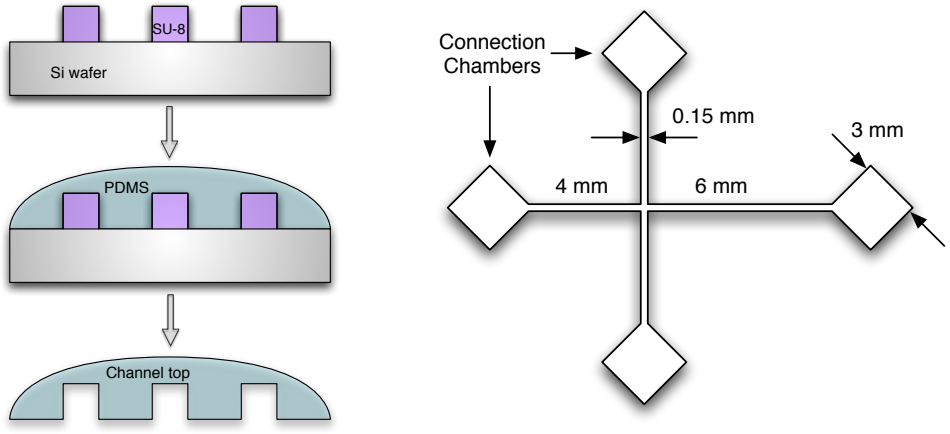

(a) Molding process (b) Channel from above

Fig. 4.4: *In (a) is a schematic illustration of the molding process, PDMS is poured onto a silicon master with a channel forming protrusion. In (b) is the channel as seen from above, with measurements of the feature sizes.*

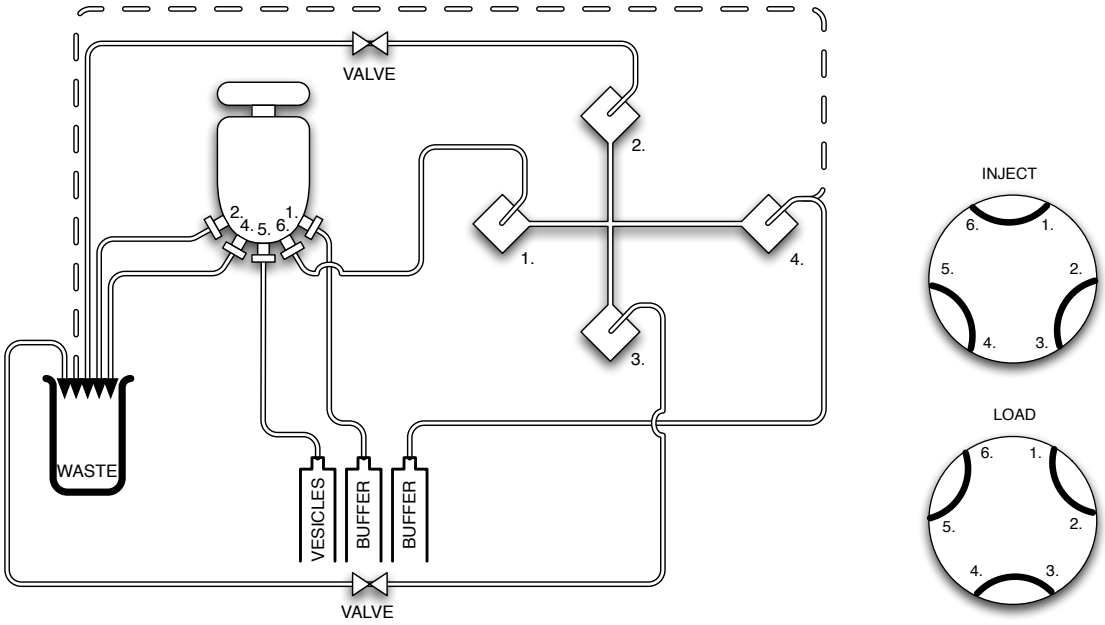

(a) (b)

Fig. 4.5: *In (a) is a schematic illustration of the experimental setup. The six-port injector valve, described in (b), can be used to easily switch between injecting, e.g., vesicles and buffer in the channel. In (b) is a description of the six-port injector valve, for instance, when in inject mode connection 1. is linked to 6., while in load mode, connection 1. is linked to 2.*

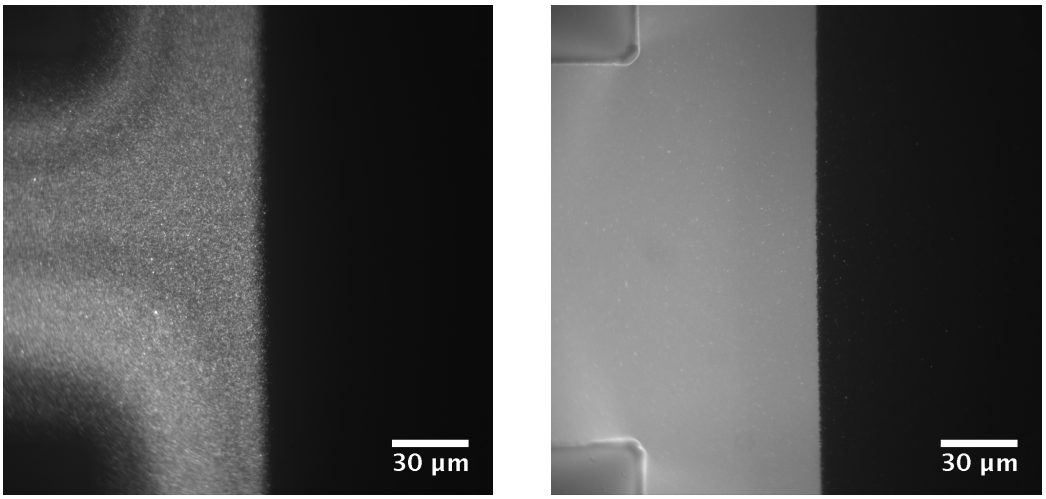

(a) Adsorbed liposomes (b) SLB formed

Fig. 4.6: *In (a) and (b) is shown fluorescence images (see below) comparing liposomes adsorbed on the surface and an SLB on the surface. Notice that the fluorescence intensity of the SLB is lower and more uniformly distributed than that of adsorbed liposomes.*

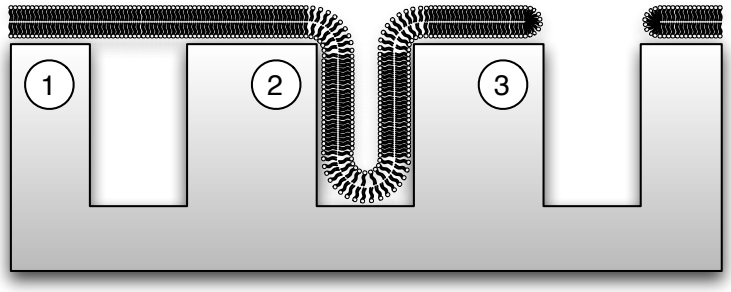

Fig. 4.7: *Schematic illustration of the three different surface coverage types discussed. (1) is the locally free spanning lipid bilayer. (2) shows a bilayer that follows the surface curvature. In (3) the bilayer has ruptured above the well.*

a bilayer on a surface where an SLB would normally not form. In the work performed in this thesis, a nanostructured surface, described previously, has been used. The aim when driving the bilayer across the nanostructured surface is to create a locally free spanning lipid bilayer[21], shown schematically in part one of Fig. 4.7, which is supported by the top surface between the wells but free hanging, spanning, across the wells. If vesicles were adsorbed directly on this structure, it is likely that the result would be a SLB on the glass support interrupted by adsorbed vesicles on the gold nanodiscs. Additionally the SLB and vesicles would be inside the wells rather than spanning.

When forming a locally free spanning lipid bilayer on the nanostructured surface, the properties of the buffer solution must be altered to provide reproducible results. When

forming a bilayer on the flat support, a buffer solution with comparatively high salt concentration (100 mM NaCl) and low pH (pH8) is used. When shear-flowing a bilayer across the nanostructure, the SLB-surface interaction must be lowered, in order for the bilayer to not follow the curvature of the surface, such as the case shown in part two of Fig. 4.7. This is achieved by lowering the salt concentration (5 mM NaCl) to increase the screening length and increasing the pH to pH9 lowering the surface-SLB interaction[21;44].

An alternative result to a locally free spanning bilayer and a bilayer following the curvature of the surface is a bilayer loosing its integrity, rupturing above the wells, shown schematically in part three of Fig. 4.7. The actual case during an experiment will probably involve all three coverages, but the aim is to predominantly have a locally free spanning lipid bilayer.

One way of determining if the bilayer is locally free spanning is to compare the drift velocity of the bilayer before and after the bilayer has entered the nanostructured area. Ideally the drift velocity should be constant if the bilayer is free spanning while it should decrease if the bilayer either follows the curvature or ruptures above the wells[21].

Another method to determine both the integrity and the spanning of the bilayer is to capture fluorescent molecules within the wells while shear-driving the bilayer[21].

4.3 Instruments

A large part of the work in this thesis has been focused on the development of a measurement setup allowing LSPR and fluorescence measurements to take place simultaneously. The setup, see Fig. 4.5, that has been used for the majority of the measurements is based on an inverted microscope suited for fluorescence measurements, with the addition of a spectrometer to perform LSPR measurements.

4.3.1 Fluorescence microscopy

Perhaps the single most important part of the combined setup is an inverted microscope (*Nikon Eclipse Ti-E*), well suited for fluorescence measurements. Fluorescence microscopy depends on the presence of fluorophores in the sample. Fluorophores are exited by a range of wavelengths roughly corresponding to the energy difference between the ground level and the first excited level, see Fig. 4.8. The excited electron then rapidly, on the order of nanoseconds, deexcites to the ground level, emitting a photon in the process. Due to vibrational relaxation, the emitted photon is usually of lower energy than the incident photon.

An SLB is usually not visible, even in a microscope. However, when measuring properties of the SLB it is often crucial to be able to image the SLB. One way of visualizing a bilayer is to incorporate lipids tagged with a fluorophore into the bilayer, often a fraction of a percent is sufficient. Using an inverted microscope the sample may be radiated from below, through the objective, by light at a wavelength specific to the fluorophore used. The fluorophore will then deexcite, emitting a photon in a random direction. Some of those emitted photons will travel through the objective to the detector, e.g. a camera or an eye, creating a signal. For a schematic illustration of a fluorescence microscopy setup, see Fig. 4.9(a).

4.3.2 Localized surface plasmon resonance

Since the aim of the thesis work is to be able to simultaneously measure both fluorescence and LSPR, the standard fluorescence microscope in Fig. 4.9(a) had to be modified. The modification is based on a flippable mirror, the use of an additional light source and an additional detector. A schematic illustration of the combined setup is shown in Fig. 4.9(b).

The additional detector is a photospectrometer (*Ocean Optics QE65000*) which is connected to the inverted microscope using an optical fiber (*Ocean Optics QP1000-2-VIS-BX*). A custom made *LabVIEW* software, as developed by Jonsson et al.[40], is used to control the spectrometer and analyze the light transmitted through the sample. The transmitted light contains information about the wavelength of maximum extinction of the sample, but the raw data first needs to be analyzed with respect to dark counts, the number of counts on the spectrometer in the absence of light, and the spectrum of the light source. When the

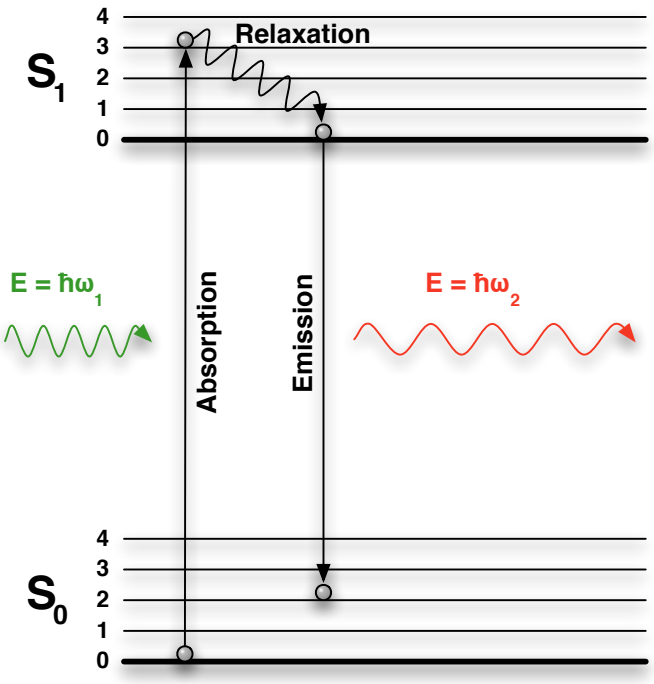

Fig. 4.8: *A Jablonski diagram of fluorescence. The process starts with excitation of one electron in the fluorophore to the excited state, S_1, by absorption of one photon. A loss of energy due to vibrational relaxation follows, and then deexitation to the ground level by emission of a photon with energy corresponding to the distance to the ground level, S_0.*

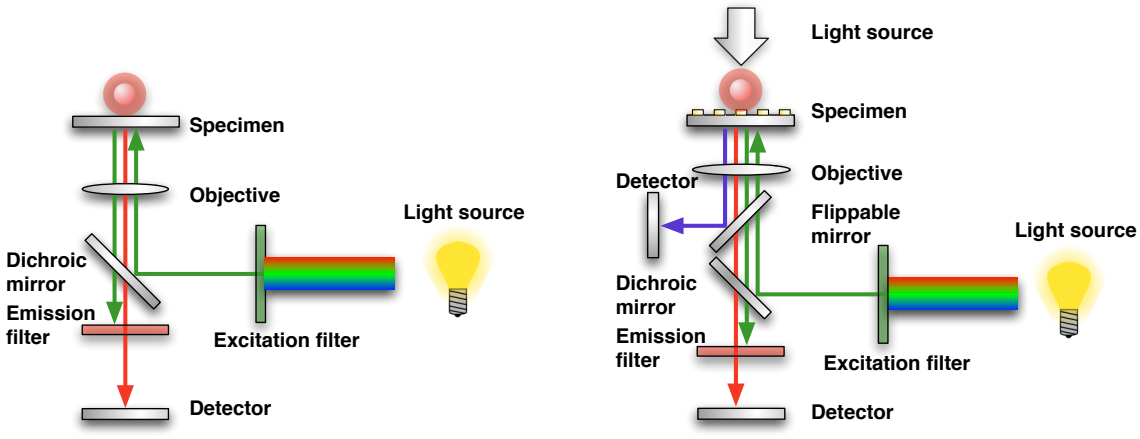

(a) Fluorescence microscope

(b) Converted for LSPR

Fig. 4.9: *Schematic illustrations of an inverted fluorescence microscope in (a) and in (b) with modifications for simultaneous fluorescence and LSPR measurements.*

corrections are made, the remaining signal will be the extinction spectrum of the sample,

$$E(\lambda) = 1 - \frac{I_{\text{sample}}(\lambda) - I_{\text{dark}}(\lambda)}{I_{\text{reference}}(\lambda) - I_{\text{dark}}(\lambda)}, \tag{4.1}$$

which can be seen in Fig. 4.3. The software fits the spectrometer data to an n:th degree polynomial, $E(\lambda) = \sum_{i=0}^{n} p_i \lambda^i$, and the position of the centroid wavelength is tracked in real time. The centroid position is used rather than the polynomial peak position since the centroid is usually a more stable signal, reducing the noise. The centroid is the center of mass of the area under the graph between two specified wave lengths, λ_a and λ_b with $E(\lambda_a) = E(\lambda_b)$, and the wave length of the centroid, λ_c, is calculated according to[46]

$$\lambda_c = \frac{\int_{\lambda_a}^{\lambda_b} \lambda \left[E(\lambda) - E(\lambda_a)\right] \mathrm{d}\lambda}{\int_{\lambda_a}^{\lambda_b} \left[E(\lambda) - E(\lambda_a)\right] \mathrm{d}\lambda}. \tag{4.2}$$

Given the polynomial approximation, $E(\lambda) = \sum_{i=0}^{n} p_i \lambda^i$, (4.2) may be simplified to an integral over a sum of polynomial coefficients

$$\lambda_c = \frac{\int_{\lambda_a}^{\lambda_b} \lambda \sum_{i=0}^{n} \left[p_i \lambda^i - p_i \lambda_a^i\right] \mathrm{d}\lambda}{\int_{\lambda_a}^{\lambda_b} \sum_{i=0}^{n} \left[p_i \lambda^i - p_i \lambda_a^i\right] \mathrm{d}\lambda}. \tag{4.3}$$

Evaluating the integrals yields the following expression for the centroid position:

$$\lambda_c = \frac{\sum_{i=0}^{n} \left[\frac{p_i}{i+2}\left(\lambda_b^{i+2} - \lambda_a^{i+2}\right) - \frac{p_i}{2}\lambda_a^i\left(\lambda_b^2 - \lambda_a^2\right)\right]}{\sum_{i=0}^{n} \left[\frac{p_i}{i+1}\left(\lambda_b^{i+1} - \lambda_a^{i+1}\right) - p_i \lambda_a^i \left(\lambda_b - \lambda_a\right)\right]}, \tag{4.4}$$

which can be monitored in real time by the custom made *LabVIEW* software. The real time monitoring enables time resolved measurements of the change in refractive index within the sensitive range of the metal nanodisc, see Fig. 4.10.

One of the most important aspects of the development of the combined fluorescence and LSPR setup was to limit and control the noise level in the LSPR measurements. The noise in the setup originates from a wide range of sources, some of them are more controllable than others.

One way to increase the signal-to-noise ratio (SNR) is to ensure that the entire dynamic range of the detector is used. The majority of the noise is either unaffected by an increase in signal strength, measured in number of captured photons, or increasing with the square

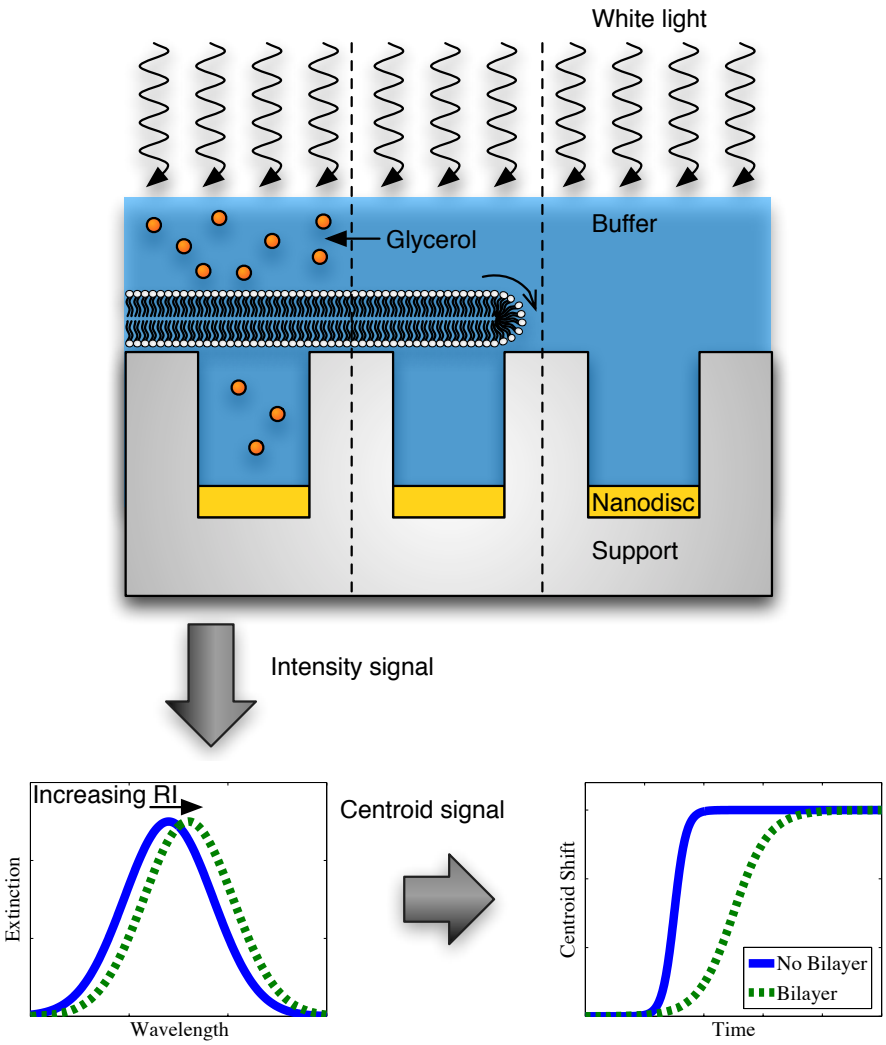

Fig. 4.10: *Schematic illustration of a transport experiment. There are three main stages: 1. With only buffer in the channel the centroid position is measured. 2. An SLB is formed in the channel and shear-driven across the nanofabricated area, forming locally free spanning SLB. 3. Glycerol is injected into the channel. Since glycerol has a larger refractive index than buffer, it will yield a LSPR shift when replacing the buffer in the vicinity of the nanodiscs. The speed and amplitude of the shift will provide information on the membranes transport properties.*

root of the number of captured photons. This means that using the entire dynamic range of the detector, there is little increase in the absolute noise level, but a clear improvement in SNR. Using the entire dynamic range of the detector may be accomplished in various ways, but corresponds to collection of more light in one way or another. The collection of light is chiefly determined by four things, the strength of the light source, the size of the sampling area, the integration time of the sensor and the sample itself.

The strength of the light source is rather self explanatory, and more light is usually better, up to the point where heat effects start to show. The size of the sampling area is rather more complicated. A larger sampling area means that more light will be collected, increasing the number of captured photons. For the rapid fluid exchange experiments performed in this thesis however, a restricted sampling area with a width smaller than half the channel width is crucial. This corresponds to finding an optimum size of the sampling area, corresponding to having a large enough sampling area to limit noise levels while being small enough for the measurements. The sampling area in itself is straight forward to calculate. The area from which light is collected on the sample will be in the shape of the optical fiber, but demagnified with the magnification of the objective, $d = D/M$, where d is the diameter if the sampling area, D is the diameter of the fiber and M is the magnification of the objective.

The same sort of conflict of interest present for the sampling area is present also for the integration time or sampling time. The longer the time, the more photons are captured, and thus an increased SNR. In order to further decrease the noise, it is possible to perform averaging on a number of outputs from the detector. In the process of noise reduction in these cases, however, measurement speed is sacrificed.

In order to conclude, reducing noise in this setup is all about making compromises. In the end, the optimum settings has been to adjust the light source in order to use the entire dynamic range of the detector while using an objective with $M = 60\,\mathrm{x}$ magnification and an optical fiber with a diameter of $D = 1000\,\mu\mathrm{m}$, yielding a sampling area with a diameter of $d = 16.67\,\mu\mathrm{m}$. With a nanodisc density of $16\,\mu\mathrm{m}^{-2}$, this corresponds to measuring on approximately 3500 discs. The integration time of the photospectrometer has generally been set to 15 ms with 10 x averaging, deemed both fast enough for the measurements performed in this thesis. Regarding both these values, they can be altered during measurements to adopt to specific needs.

Chapter 5:
Towards transport measurements

In this chapter the results acquired during the course of this thesis are presented. The experiments are divided into subgroups corresponding to either mastering known techniques or the characterization of the new combined LSPR and fluorescence microscopy setup and the nanofabricated chips.

5.1 LSPR properties of metal nanodics

The LSPR samples has been fabricated using a range of differently sized gold nanodiscs in the bottom of wells, all with a diameter of 110 nm, but with thicknesses varying between 15 and 35 nm. The different nanodiscs have been characterized with respect to wavelength of maximum extinction, centroid wavelength, λ_c, and extinction. The spectrum of one of each disc size manufactured during the thesis is shown in Fig. 5.1(a). The corresponding average centroid position of manufactured samples can be seen in Fig. 5.1(b). Outliers has been removed from the data since it is believed that these are the result of an error in the manufacturing process. The centroid position as a function of disc thickness is almost linear, which is to be expected from the theory[47]. Also, the results presented in Fig. 5.1(b) correspond rather well with previous findings[48;49].

The spectrum of the light incident on the sample is shown in Fig. 5.1(c). As can be seen it does not have the spectrum of an ideal black body radiator, since there is no intensity above 800 nm. With the light source being a tungsten halogen lamp, this means that the spectral properties of the various filters and lenses within the microscope intervene. Maximum intensity from the light source is at ~ 670 nm.

Given the spectral properties of the light source and the transmitting properties of the various lenses present in the LSPR setup, the most suitable disc thickness should correspond to a wavelength of maximum extinction and centroid wavelength at around 670 nm. For this thesis a thickness of 30 nm was chosen, corresponding to $\lambda_c \approx 650$ nm.

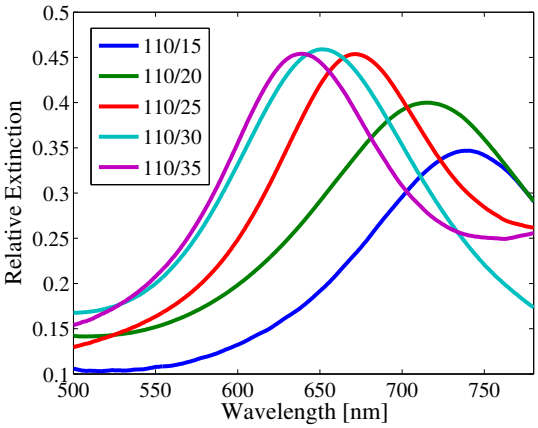

(a) LSPR spectra

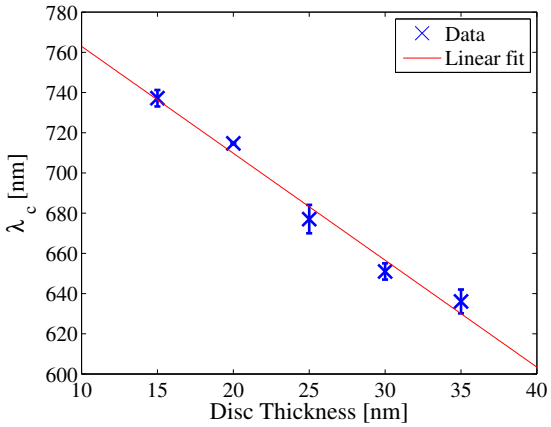

(b) Centroid position

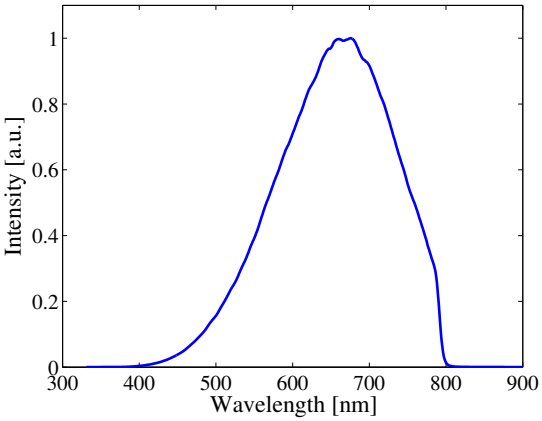

(c) Light source spectrum

Fig. 5.1: *In (a) is the extinction spectra for samples with ⌀ 110 nm discs of varying thickness shown. In (b) is shown the corresponding centroid position with error bars. The plotted values are averages of three or more manufactured samples. The spectrum of the light incident on the sample is shown in (c).*

5.2 Shear-driven lipid bilayers

Since it is not possible to form a locally free spanning SLB on the nanostructured surface by injection of vesicles, the concept of shear-driven bilayers has been central to the work in this thesis. When shear-driving an SLB over a surface, a rather high bulk flow rate, more exactly 250 µl/min for the work in this thesis, is used to get the bilayer moving. As previously described, the front of a shear-driven bilayer has a characteristic shape, shown in Fig. 5.2, predicted by fluid dynamics[17]. The bilayer front forms a parabola corresponding to the flow speed being larger in the middle than at the sides in the square channel[17]. There is also an accumulation of larger molecules in the bilayer front, as discussed in chapter 2.

When the bilayer is shear-driven across a surface it will have a certain drift velocity. This drift velocity is mainly dependent on the bulk flow speed and the bilayer-surface interaction. The first parameter is straight forward, a higher flow speed means a larger drift velocity. The latter is influenced by many different things, e.g. the salt concentration in the buffer solution, larger salt concentration leads to more screening, thus a shorter Debye length. As previously discussed, the pH of the buffer solution will also impact the bilayer-surface interaction. The drift velocity can also differ slightly between samples, so it is not readily comparable between samples, however, given the same conditions regarding for instance the channel size and buffer used, it will be similar. On a flat surface in a microfluidic chip with a cross section of 150×113 µm, the drift velocity was measured to be approximately 0.23 µm/s with a bulk flow of 250 µl/min, see Fig. 5.3.

As described previously the drift velocity can be used to determine whether a shear-driven bilayer is locally free spanning or not when advancing across the nanostructured surface. If the bilayer follows the curvature of the surface it travels a longer distance for a given projected area than it would have done if the surface was flat. Thus the observed drift velocity will decrease.

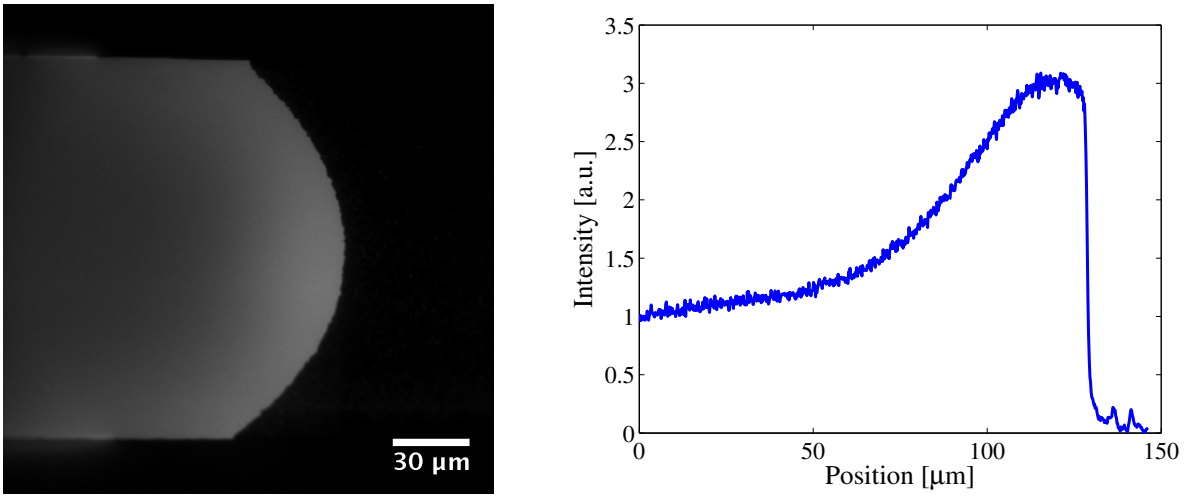

(a) Fluorescence image

(b) Intensity profile

Fig. 5.2: *A shear-driven lipid bilayer. The front of the shear-driven bilayer has a characteristic shape, predicted by fluid dynamics. From the intensity profile, along the middle of the fluorescence image in (a), shown in (b) it is clear that there is an accumulation of the larger fluorescence tagged molecules in the bilayer front.*

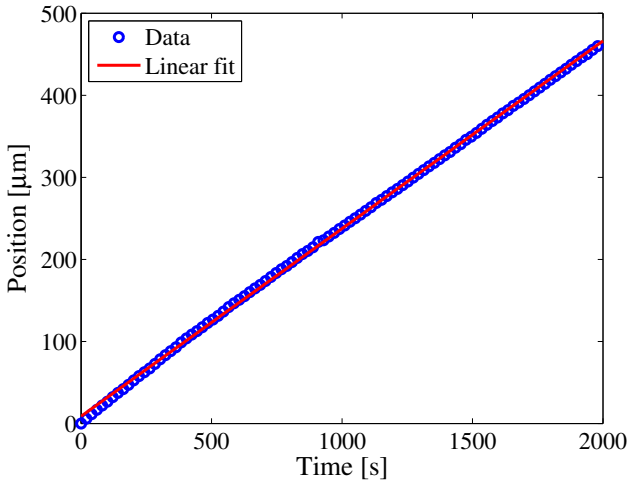

Fig. 5.3: *The distance covered by the bilayer inside a microfluidic chip in 20 s intervals with a bulk flow velocity of 250 µl/min. Linear interpolation gives 0.23 µm/s as the average drift velocity.*

5.3 Fluid exchange

In order to investigate the sensitivity of the nanofabricated chips to changes in the refractive index of the liquid in the vicinity of the nanodiscs, the setup in Fig. 4.5 was modified to the one seen in Fig. 5.4. This setup has been optimized so that the fluid in the measurement area of the channel can be exchanged rapidly. Turning the six-port injector valve from load to inject will shift the glycerol from the lower half of the channel, to the upper. Since the measurement area is on the order of a tenth of the channel width, as discussed in chapter 4, this means that the fluid in the measurement area, located approximately 1/4 from the channel wall, will change very quickly. In the future, this setup will be implemented into the experimental setup in Fig. 4.5. This can be achieved by the addition of a second six-port injection valve implemented in the same manner as the one in Fig. 5.4. The combination of the fast fluid exchange setup and the bilayer forming setup enables rapid changes of the fluid above the bilayer in future transport measurements.

The fluids used to investigate the sensitivity of the chips was water and water with different mass percentages of glycerol. As can be seen in Tab. 5.1, even a change from water to 5 *wt*% glycerol produces a clear contrast in refractive index. This difference is larger the larger the mass percentage of glycerol. Too large steps in glycerol concentration may compromise the fluid exchange in the channel, due to the large difference in viscosity, see Tab. 5.2.

Tab. 5.1: *The refractive index at 20°C of different mass percentages (mp) of glycerol in water*[50].

mp	***n***
0	1.3330
5	1.3388
10	1.3448
15	1.3511
20	1.3575
25	1.3640
30	1.3707

Tab. 5.2: *Comparison of the density and viscosity at 20°C of water and 5, 30 and 100 wt% glycerol*[51].

mp	$\boldsymbol{\rho}$ [g cm^{-3}]	$\boldsymbol{\eta}$ [mPa s]
0	0.9982	1.002
5	1.0097	1.145
30	1.0717	2.505
100	1.2611	1460.0

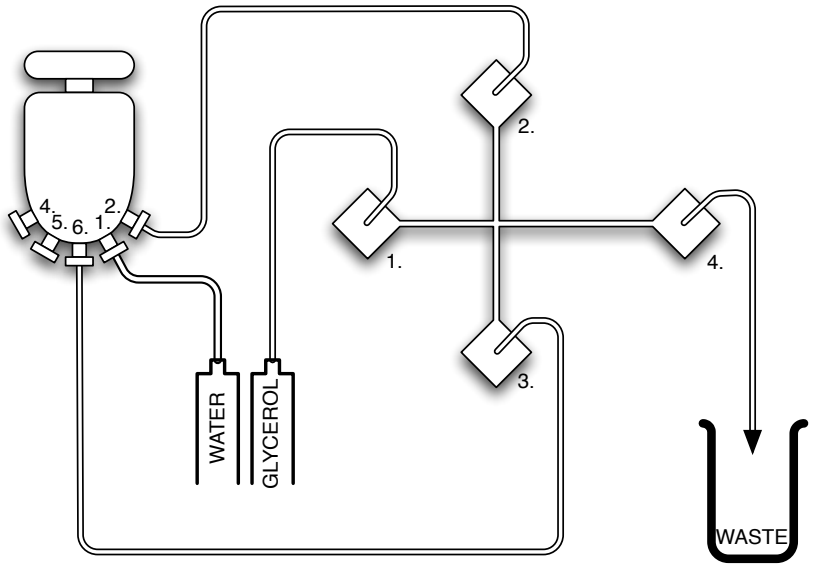

Fig. 5.4: *The setup used to change fluid in the microfluidic channel rapidly, compare to Fig. 4.5. Turning the six-port injector valve from load to inject will shift the water flow from connection 2. to 3. which will move the glycerol flow from the lower part of the channel to the upper. Since the measurement area is only* $10 - 20\,\mu m$ *wide, this will rapidly change the fluid in the measurement area.*

5.4 Sensitivity of the nanofabricated surfaces

The setup described in the previous section was used to measure the performance of the nanofabricated chips. Measuring the performance means to measure the centroid shift when switching between solutions with known refractive indices. The result is a sensitivity plot with entries corresponding to each of the measurements. These data points can then be interpolated to give a measure of the sensitivity in [nm/refractive index unit (RIU)].

Fig. 5.5(a) shows such a measurement, switching back and forth between water and different solutions of water and $5 - 30\,wt\%$ glycerol, with known refractive indices, see Tab. 5.1. The trace corresponding to $30\,wt\%$ is a little bit unstable, which corresponds to the large viscosity contrast between this solution and pure water.

From the traces in Fig. 5.5(a) it is also possible to determine the rise time, defined as the time required for a signal to change from $10-90\,\%$ of the maximum signal, $t_r = t_{90\%} - t_{10\%}$. The rise time differs between 0.4 s and 0.8 s, with lower glycerol concentrations yielding a shorter rise time. This can probably be related to the difference in viscosity.

Comparing the water level with the level corresponding to the respective glycerol solutions and plotting the difference in centroid position as a function of diffractive index yields Fig. 5.5(b). From a linear fit of the data points the sensitivity of this nanoplasmonic surface was calculated to be 67.5 nm/RIU.

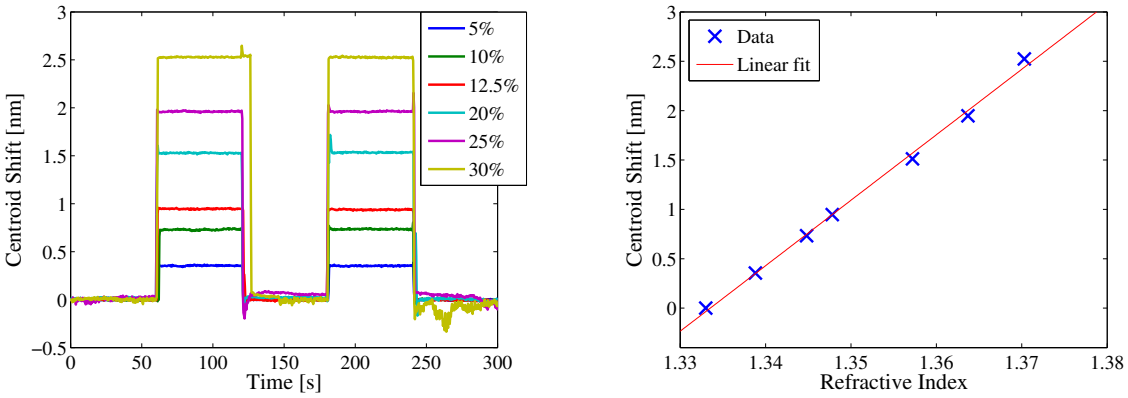

(a) Centroid shift (b) Sensitivity

Fig. 5.5: *In (a), the centroid shift switching back and forth between water and* $5 - 30\,wt\%$ *glycerol, using the setup described in Fig. 5.4. In (b) the sensitivity as calculated from measurements in (a). A linear fit of result yields 67.5 nm/RIU.*

5.5 Combining LSPR and fluorescence microscopy

The aim of this thesis has been to measure transport across cell membrane mimics. In order to do so, a setup has been built with which it is possible to simultaneously measure fluorescence and LSPR. The advantage of measuring both fluorescence and LSPR simultaneously is the possibility to see what happens with the bilayer via fluorescence at the same time as studying e.g. the transport of something across the membrane with LSPR. Such measurements are work in progress at the moment.

The combined setup was used for simultaneous measurements when driving a bilayer across the nanostructured surface and when injecting POPC vesicles into the channel, see Fig. 5.6 and 5.7. Fig. 5.6 shows the border between the nanostructured and the flat surface, seen as a shift in brightness of the surface, before, Fig. 5.6(a). and after, Fig. 5.6(b) a bilayer has been shear-driven across it.

Fig. 5.7(a) shows the centroid shift when injecting 1 mg/ml POPC with $0.1\,wt\%$ R-DHPE vesicles at a rate of $10\,\mu$l/min. This figure can be compared with previous findings of Jonsson et al.[38], which showed that the centroid shift is accelerated when the vesicles burst and merge into a bilayer. In Fig. 5.7(a) however, no such acceleration is measured. This implies that the majority of the vesicles do not rupture in the vicinity of the gold nanodiscs. This is to be expected, since SLB do not form on gold surfaces[20]. The end result, seen in Fig. 5.7(b), may be an SLB on the nanostructured surface, interrupted by adsorbed vesicles on the gold nanodiscs. Further investigations including a fluorescence recovery after photobleaching (FRAP) measurement are needed to clarify what happens. It should also be noted that since the nanodiscs are sensitive some distance away from the surface, corresponding to the walls of the wells, one could argue that an acceleration in the centroid shift signal due to vesicle rupture at the walls should be visible in Fig. 5.7(a).

However, since the binding process in Fig. 5.7(a) is slow, the acceleration may be hidden by other processes within the signal.

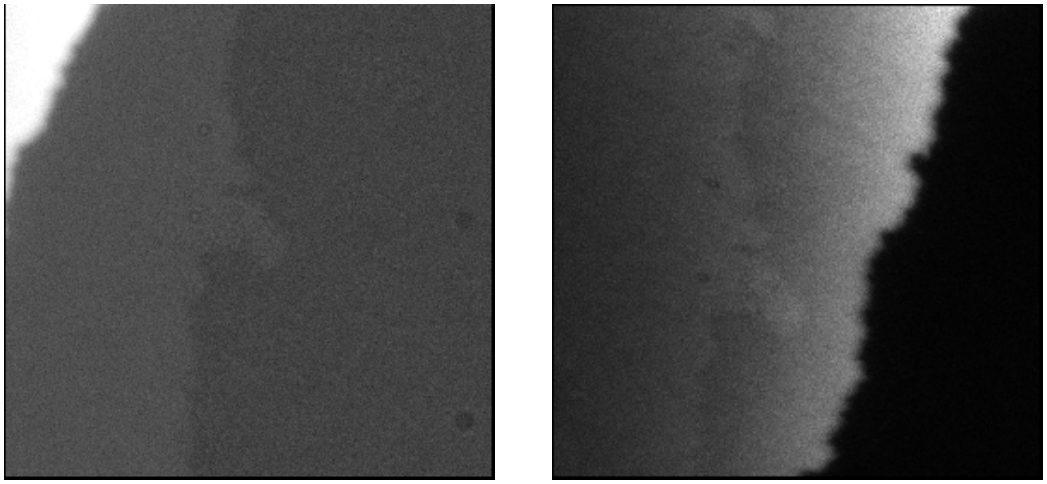

(a) Before (b) After

Fig. 5.6: *The border between the nanofabricated area and the flat support, before (a) and after (b) the bilayer has passed. Note that the gray levels are not comparable between the images.*

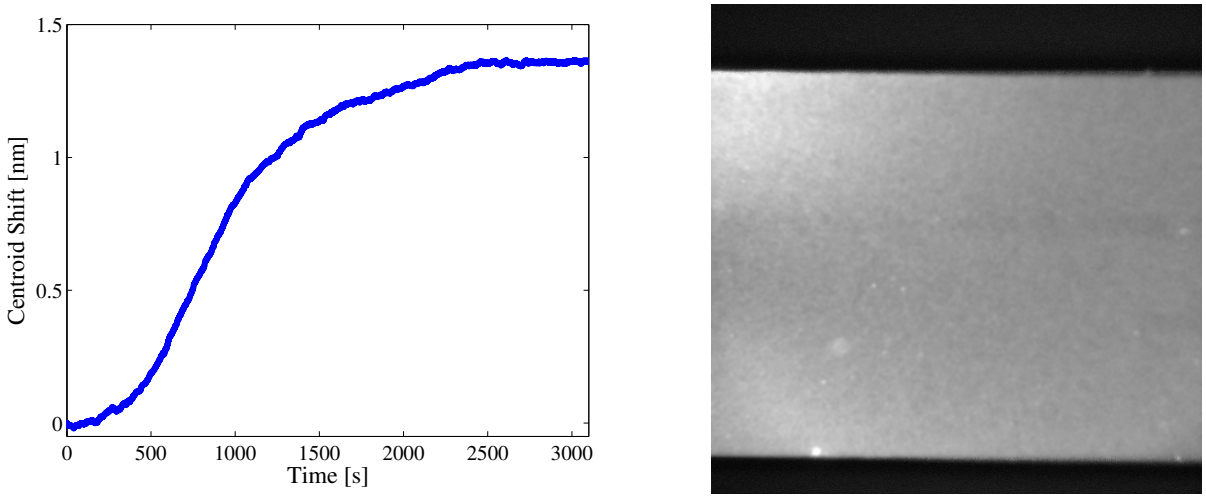

(a) Centroid signal (b) Fluorescence image

Fig. 5.7: *In (a) is the centroid shift as 1 mg/ml POPC with 0.1 wt% R-DHPE vesicles are injected into the channel at 10 µl/min. In (b) is a fluorescence image of the area from which the trace in (a) was obtained. The uniform intensity suggest that an SLB is formed. However, from the trace it is likely that there is only vesicles adsorbing to the gold discs. This would correspond to the SLB not being complete. Further investigations are needed, for instance a FRAP measurement.*

Chapter 6:
Improvements and outlook

During the thesis, a new setup has been developed, and many issues on the way towards transport measurements have been resolved. One major issue that is yet to be resolved ahead of measurements is the formation of a locally free spanning SLB on the nanofabricated surface. Since this is something that has previously been achieved on similar surfaces[21], it can most definitely be done.

Having said that, in the future, when measuring transport properties of the SLB it may not be ideal to use the glycerol solutions that have been used in order to study the sensitivity of the surfaces since adding glycerol into the system may result in an osmotic stress on the membrane which may cause it to burst. What may instead be used is buffer solutions based on heavy water, i.e. water where the hydrogen atoms are replaced with deuterium. A change from water to heavy water should not be detected by the membrane but there is a clear contrast in refractive index making it possible to measure the transport properties.

Moving on, there are a number of experiments that must be performed to gain more knowledge of the system. Probably the most crucial of them is a measurement of the diffusivity of the SLB, using, e.g. FRAP. Diffusivity measurements yields information about whether there is actually a bilayer on the surface and about the state of the bilayer, for instance whether there are immobile fractions. Diffusivity measurements are of interest to carry out both on different parts of the surface, but also in different buffer solutions with altering pH and salt concentration. An improvement of the combined LSPR and fluorescence microscopy setup will therefore be to also implement the equipment necessary for FRAP measurements. Of equal importance as the diffusivity is a wider knowledge of the drift velocity, also as a function of different parts of the surface and different buffer solutions.

While on the subject of learning more about the system, measurements using other sizes of plasmonic nanoparticles are also of interest, characterizing the optimum sensitivity. The main reason for using 110/30 nm discs, as stated before, have been that the centroid position and therefore the wavelength of maximum extinction of such discs is approximately the same as the wavelength of peak intensity of the light source in the setup. Using thinner discs corresponds to a redshift of the centroid position and the longer the wavelength the larger the corresponding centroid shift for a given change in refractive index, though this may mean a need to replace the light source and the various lenses and filters in the setup.

Thinner discs also mean that the peak will be slightly wider, thus it is of interest to compare the performance of chips with, for instance, 110/30 nm and 110/20 nm discs.

The microfluidic chips could be reused around three times, before the surface was too contaminated for a SLB to form. This is an improvement compared with the same type of nanostructure fabricated using a similar, but slightly different procedure (Jonsson et al., in preparation). The microfluidic chips could, however, not withstand a more thorough cleaning procedure, using sonication, since sonication remove the gold nanodiscs. This is the cleaning procedure usually performed on non-nanostructured chips, and significantly increase the life time of the chips. The problem can probably be traced to the use of chromium not only as an etch mask, but also as an adhesion layer for the gold. The idea is that the thin chromium layer is not reached by the chromium etch, only the etch mask is removed, but the fact that the discs is set loose by the sonication in the cleaning regime may suggest otherwise. The immediate answer to this problem is to change gold adhesion layer from chromium to titanium, which is unaffected by the chromium etch. This will however change the plasmon properties of the samples, thus the results will not be immediately comparable.

For the future, the system can be used to investigate more complex systems than a bilayer formed by just two lipids. Perhaps the first step is to incorporate proteins in the bilayer, either simple pores like some poisons, or ion channels. The ion channels however may need an electrical potential to work as intended, thus requiring the addition of electrodes in the chips. Later, measuring on real biological membranes originating from cells should not be impossible. While vesicles formed from real cell membranes will not merge into a lipid bilayer, if an SLB is shear-driven into the vesicles the SLB and vesicles will merge, thus producing an SLB model system more similar to a real biological membrane.

Measuring transport across any of these membranes will yield a better understanding of the properties of membranes and membrane proteins. Looking further ahead, using a biological membrane SLB, it may be possible to study the influence of different protein-targeting drugs on transport properties.

Acknowledgements

I owe a lot to coworkers, fellow students, friends and family for helping me solve various problems that I have encountered during the work I have done in this thesis. This thesis would not have been possible without you.

My supervisors, *Peter Jönsson* and *Magnus Jonsson* deserve a special mention for all their support and help they have provided me during my work. Thank you for guiding me through the sometimes muddy waters of microfluidics, shear-driven bilayers and nanoplasmonics. Magnus, if it wasn't for you I would not have seen the Lycurgus cup and I am sincerely sorry for not noticing your kink earlier. Peter, as the inventor of the shear-driven bilayer, this thesis would never have been done without your work. I also believe that the feedback you two have provided have greatly improved this thesis.

My examiner, *Fredrik Höök*, thank you for the inspiration you have given me, the discussions we have had and the feedback you have provided. I do hope that our discussions on the subject of running have actually turned you into a better runner.

Francesco Mazzotta and *Laurent Feuz*, thank you for helping me out in the cleanroom with the SEM and other equipment that a M.Sc. student is not allowed to operate, and for helping me with various aspects of LSPR after Magnus left Göteborg.

Thomas Olsson, for the many rewarding discussions on the most different of subjects, but perhaps particularly those regarding our thesis work.

Anders Lindman and *Nils Jungenfelt* for lunch and coffee break company.

Kristian Dimitrievski for you sharing your room with me, and the many discussions we have had during this half year. Without you, I would still not know what h-index is.

I would also like to thank the coworkers at biological physics, not least since you, through the means of bio-sport, have enabled me to prove to the world that I really can not do sports involving balls.

Last but not least, I would like to thank my family for their love and support.

My apologies if I have inadvertently omitted anyone to whom acknowledgement is due.

At the end of things, none of the above mentioned can be held responsible for what is written in this report, for that I take full responsibility. Having said that, the people mentioned above should take full credit for their contribution to my work, where there are errors, omissions and over-simplifications, it is probably because I did not heed their advice fully enough.

Thank you.

Bibliography

[1] Phillips, R., Kondev, J. & Theriot, J. *Physical Biology of the Cell* (Garland Science, New York, NY, 2009), 1. edn.

[2] Alberts, B. *et al. Molecular Biology of the Cell* (Garland Science, New York, NY, 2007), 5. edn.

[3] Lundstrom, K. *Cell. Mol. Life Sci.* **63**, 2597–2607 (2006).

[4] Tanaka, M. & Sackmann, E. *Nature* **437**, 656–663 (2005).

[5] Sackmann, E. *Science* **271**, 43–48 (1996).

[6] Jönsson, P., Beech, J. P., Tegenfeldt, J. O. & Höök, F. *J. Amer. Chem. Soc.* **131**, 5294–5297 (2009).

[7] Jo, B.-H., Van Lerberghe, L. M., Motsegood, K. M. & Beebe, D. J. *J. Microelectromech. S.* **9**, 76–81 (2000).

[8] Atencia, J. & Beebe, D. J. *Nature* **437**, 648–655 (2005).

[9] Maier, S. A. *Plasmonics: Fundamentals and Applications* (Springer, New York, NY, 2007).

[10] Brändén, M., Tabaei, S. R., Fischer, G., Neutze, R. & Höök, F. *Biophys. J.* **99**, 124–133 (2010).

[11] van Meer, G. *EMBO J.* **24**, 3159–3165 (2005).

[12] Jones, R. A. L. *Soft Condensed Matter* (Oxford University Press, Oxford, 2002), 1. edn.

[13] Alexandridis, P., Zhou, D. & Khan, A. *Langmuir* **12**, 2690–2700 (1996).

[14] Israelachvili, J. N. *Intermolecular and Surface Forces* (Academic Press, Burlington, MA, 2011), 3. edn.

[15] McConnell, H. M., Watts, T. H., Weis, R. M. & Brian, A. A. *Biochim. Biophys. Acta* **864**, 95–106 (1986).

[16] Plant, A. L. *Langmuir* **9**, 2764–2767 (1993).

[17] Jönsson, P. & Höök, F. *Langmuir* **27**, 1430–1439 (2011).

[18] Day, M. A. *Erkenntnis* **33**, 285–296 (1990).

[19] Jönsson, P., Gunnarsson, A. & Höök, F. *Anal. Chem.* **83**, 604–611 (2011).

[20] Keller, C. A. & Kasemo, B. *Biophys. J.* **75**, 1397–1402 (1998).

[21] Jönsson, P., Jonsson, M. P. & Höök, F. *Nano Lett.* **10**, 1900–1906 (2010).

[22] Hummel, R. E. *Electronic Properties of Materials* (Springer, New York, NY, 2000), 3. edn.

[23] Linden, S. *et al. Science* **306**, 1351–1353 (2004).

[24] Ritchie, R. H. *Phys. Rev.* **106**, 874–881 (1957).

[25] Kretschmann, E. & Raether, H. *Z. Naturforsch. Pt. A* **23**, 2135–2136 (1968).

[26] Otto, A. *Z. Phys.* **216**, 398–410 (1968).

[27] Zayats, A. V., Smolyaninov, I. I. & Maradudin, A. A. *Phys. Rep.* **408**, 131–314 (2005).

[28] Studer, A., Han, X., Winkler, F. K. & Tiefenauer, L. X. *Colloid Surface B* **73**, 325–331 (2009).

[29] Haes, A. J. & Richard P. Van Duyne. *Anal. Bioanal. Chem.* **379**, 920–930 (2004).

[30] Myroshnychenko, V. *et al. Chem. Soc. Rev.* **37**, 1792–1805 (2008).

[31] Lal, S., Link, S. & Halas, N. J. *Nat. Photonics* **1**, 641–648 (2007).

[32] Anker, J. N. *et al. Nat. Mater.* **7**, 442–453 (2008).

[33] Kvasnicka, P. & Homola, J. *Biointerphases* **3**, FD4–FD11 (2008).

[34] Link, S. & El-Sayed, M. A. *J. Phys. Chem. B* **103**, 8410–8426 (1999).

[35] Huang, X., Neretina, S. & El-Sayed, M. A. *Adv. Mater.* **21**, 4880–4910 (2009).

[36] Eustis, S. & El-Sayed, M. A. *Chem. Soc. Rev.* **35**, 209–217 (2006).

[37] Stewart, M. E. *et al. Chem. Rev.* **108**, 494–521 (2008).

[38] Jonsson, M. P., Jönsson, P., Dahlin, A. B. & Höök, F. *Nano Lett.* **7**, 3462–3468 (2007).

[39] Jonsson, M. P., Dahlin, A. B., Jönsson, P. & Höök, F. *Biointerphases* **3**, FD30–FD40 (2008).

[40] Jonsson, M. P., Dahlin, A. B., Feuz, L., Petronis, S. & Höök, F. *Anal. Chem.* **82**, 2087–2094 (2010).

[41] Willets, K. A. & Van Duyne, R. P. *Ann. Rev. Phys. Chem.* **58**, 267–297 (2007).

[42] Burda, C., Chen, X., Narayanan, R. & El-Sayed, M. A. *Chem. Rev.* **105**, 1025–1102 (2005).

[43] Feuz, L., Jönsson, P., Jonsson, M. P. & Höök, F. *ACS Nano* **4**, 2167–2177 (2010).

[44] Cremer, P. S. & Boxer, S. G. *J. Phys. Chem. B* **103**, 2554–2559 (1999).

[45] Jönsson, P., Beech, J. P., Tegenfeldt, J. O. & Höök, F. *Langmuir* **25**, 6279–6286 (2009).

[46] Dahlin, A. B., Tegenfeldt, J. O. & Höök, F. *Anal. Chem.* **78**, 4416–4423 (2006).

[47] Miller, M. M. & Lazarides, A. A. *J. Phys. Chem. B* **109**, 21556–21565 (2005).

[48] Hanarp, P., Käll, M. & Sutherland, D. S. *J. Phys. Chem. B* **107**, 5768–5772 (2003).

[49] Mazzotta, F., Wang, G., Hägglund, C., Höök, F. & Jonsson, M. P. *Biosens. Bioelectro.* **26**, 1131–1136 (2010).

[50] Hoyt, L. F. *Ind. Eng. Chem.* **26**, 329–332 (1934).

[51] "Concentrative properties of aqueous solutions: density, refractive index, freezing point depression, and viscosity," in *CRC Handbook of Chemistry and Physics* (CRC Press/-Taylor and Francis, Boca Raton, FL, 2011), W. M. Haynes, ed., 91. edn. (Internet Version).

Appendix A:
Fabrication of nanowells

Material

- ◇ Glass slides, (#2: 0.2 mm in thickness, ⌀25 mm, Menzel-Gläser, Braunschweig, Germany).

Cleaning (Wet benches)

- ◇ Sonicate in acetone ($OC(CH_3)_2$) for three minutes.
- ◇ Sonicate in IPA (propan-2-ol, $(CH_3)_2CHOH$) for three minutes.
- ◇ Oxygen plasma cleaning (TePla 300PC, tool #228). 1 kW, 2 min.

Deposit SiO_2 (STS PECVD, tool #303)

- ◇ PECVD of a ∼300 nm thick layer of SiO2 in 10 minutes.

Add colloids (Wet benches)

- ◇ Charge surface of the glass slide by adding aluminum chlorohydrate (ACH) to the surface and incubate for one minute.
- ◇ Rinse with water for one minute. Blow dry with nitrogen.
- ◇ Add colloids (1 wt% 110 nm polystyrene in MilliQ™(Millipore, Billerica, MA, USA)) to the surface. Let incubate for one minute.
- ◇ Rinse with water for one minute. Blow dry.

Tape lift-off 1

- ◇ Partial tape lift-off using clean room tape to remove colloids from one half of the glass slide.

Evaporation 1 (Edwards Auto 306, tool #425)

- ◇ 25 nm thick layer of chromium

Tape lift-off 2

- ◇ Full tape lift-off to remove the remaining colloids

Etching (Oxford Plasma Technology Plasmalab 100, tool #404)

- ◇ RIE using NF_3-gas. Etching for 3 min yields ∼200 nm deep wells.

Evaporation 2 (Edwards Auto 306, tool #425)

- ◇ 1 nm thick layer of chromium to ensure binding of gold in the bottom of the wells.
- ◇ 30 nm thick layer of gold.

Chromium etching (Wet benches)

- ◇ Place the samples in chromium wet etch over night. This dissolves the chromium everywhere on the samples but the bottom of the wells. The chromium deposited in the bottom of the wells will not be in contact with the etch fluid. Rinse with IPA and blow dry.

Appendix B:
Making a microfluidic channel

Making the PDMS

- ◇ Pour $3 - 4\,\mathrm{g}$ of PDMS (Sylgaard 184, Dow Corning, Midland, MI, USA) from the bottle.
- ◇ Add $1/10 \cdot 3 - 4\,\mathrm{g}$ curing agent (Dow Corning, Midland, MI, USA) from the drop bottle, and mix carefully.
- ◇ Put the mix into the vacuum pump for at least 15 min or until there are no bubbles left in the PDMS.
- ◇ Blow the master clean with N_2.
- ◇ Place the master on a plastic cap, and pour PDMS onto the master.
- ◇ Bake the sample in an oven at 95 °C for at least an hour.

Preparing the nanofabricated glass slide

- ◇ Place the glass slide in acetone for 5-10 min, rinse with IPA.
- ◇ Place the glass slide in IPA for 5-10 min, rinse with IPA.
- ◇ Rinse thoroughly with MilliQ™(Millipore, Billerica, MA, USA) water, place the glass slide in the oven to dry at 150 °C for 30 min.
- ◇ Remove any organic residues from the surface using oxygen plasma cleaner (PDC-32G Plasma Cleaner, Harrick Plasma, Ithaca, NY, USA). This also negatively charges the surface, making it more reactive.

Finalizing the microfluidic channel

- ◇ Drill holes in the PDMS at the connection chambers.
- ◇ Remove extra PDMS so that the channel fits the glass slide.
- ◇ Put the PDMS, bottom up, in the plasma cleaner to make the surface bond to the glass slide and to remove any organic residues.
- ◇ Briefly put the channel in the oven, to ensure a better bond.

- ◇ Put the PDMS on the glass slide, add some water at the connection chambers. Capillary forces will fill the channel with water. (Needed for the channel to remain hydrophilic).
- ◇ Cut approximately 1.5 cm long pieces of silicone tubing ID 1.5 mm, one for each connection. Rinse with MilliQ™and blow dry with N_2.
- ◇ Attach the silicone tubing to the connection with silicone adhesive (Elastosil AO7, RTV-1 silicone rubber, Wacker Silicones, Munich, Germany).
- ◇ Cure the adhesive in humid air for 45 min.